Article

Developmental Cell

Serial Synapse Formation through Filopodial Competition for Synaptic Seeding Factors

Graphical Abstract

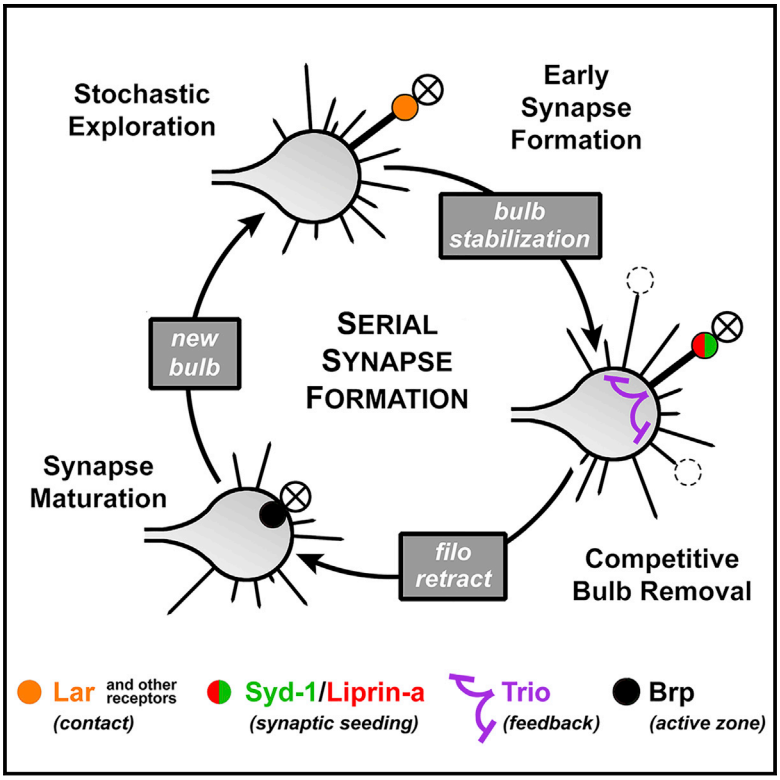

Authors

M. Neset Özel, Abhishek Kulkarni, Amr Hasan, ..., Steffen Prohaska, Max von Kleist, P. Robin Hiesinger

Correspondence

robin.hiesinger@fu-berlin.de (P.R.H.), vkleist@zedat.fu-berlin.de (M.v.K.)

In Brief

How random axon filopodia dynamics lead to precise numbers of synaptic contacts during development is unknown. Özel et al. show, through live imaging and computational modeling, that a "winner-takes-all" distribution of synaptic seeding factors renders one filopodium at a time synaptogenic, thereby pacing development and ensuring robust connectivity.

Highlights

- Stochastic filopodia dynamics are required for robust synapse formation in fly brains
- Only 1–2 filopodia at a time contain synaptic seeding factors and are synaptogenic
- 4D tracking and computational modeling support a serial synapse formation model
- Synapse formation prevents axonal retraction

Özel et al., 2019, Developmental Cell *50*, 1–15
August 19, 2019
https://doi.org/10.1016/j.devcel.2019.06.014

CellPress

Please cite this article in press as: Özel et al., Serial Synapse Formation through Filopodial Competition for Synaptic Seeding Factors, Developmental Cell (2019), https://doi.org/10.1016/j.devcel.2019.06.014

Developmental Cell
Article

Serial Synapse Formation through Filopodial Competition for Synaptic Seeding Factors

M. Neset Özel,[1,2,6,8] Abhishek Kulkarni,[1,6] Amr Hasan,[1,6] Josephine Brummer,[3] Marian Moldenhauer,[4,5,9] Ilsa-Maria Daumann,[1] Heike Wolfenberg,[1] Vincent J. Dercksen,[3] F. Ridvan Kiral,[1] Martin Weiser,[4] Steffen Prohaska,[3] Max von Kleist,[5,7,9,*] and P. Robin Hiesinger[1,7,10,*]

[1]Division of Neurobiology, Institute for Biology, Freie Universität Berlin, 14195 Berlin, Germany
[2]Neuroscience Graduate Program, UT Southwestern Medical Center Dallas, Dallas, TX 75390, USA
[3]Department of Visual Data Analysis, Zuse Institute Berlin, 14195 Berlin, Germany
[4]Computational Medicine and Numerical Mathematics, Zuse Institute Berlin, 14195 Berlin, Germany
[5]Department of Mathematics and Informatics, Freie Universität Berlin, 14195 Berlin, Germany
[6]These authors contributed equally
[7]Senior author
[8]Present address: Department of Biology, New York University, New York, NY 10003, USA
[9]Present Address: MF1, Robert Koch-Institut, Nordufer 20, 13353 Berlin
[10]Lead Contact
*Correspondence: robin.hiesinger@fu-berlin.de (P.R.H.), vkleist@zedat.fu-berlin.de (M.v.K.)
https://doi.org/10.1016/j.devcel.2019.06.014

SUMMARY

Following axon pathfinding, growth cones transition from stochastic filopodial exploration to the formation of a limited number of synapses. How the interplay of filopodia and synapse assembly ensures robust connectivity in the brain has remained a challenging problem. Here, we developed a new 4D analysis method for filopodial dynamics and a data-driven computational model of synapse formation for R7 photoreceptor axons in developing *Drosophila* brains. Our live data support a "serial synapse formation" model, where at any time point only 1–2 "synaptogenic" filopodia suppress the synaptic competence of other filopodia through competition for synaptic seeding factors. Loss of the synaptic seeding factors Syd-1 and Liprin-α leads to a loss of this suppression, filopodial destabilization, and reduced synapse formation. The failure to form synapses can cause the destabilization and secondary retraction of axon terminals. Our model provides a filopodial "winner-takes-all" mechanism that ensures the formation of an appropriate number of synapses.

INTRODUCTION

After pathfinding, axon growth cones transition to become terminal structures with presynaptic active zones. How axon terminals form a defined number of synaptic contacts with a specific subset of partners is a daunting problem in dense brain regions (Sanes and Yamagata, 2009; Yogev and Shen, 2014). Stochastically extending and retracting filopodial extensions occur during both pathfinding (Chien et al., 1993; Mason and Erskine, 2000) and synapse formation (Özel et al., 2015) and are thought to facilitate interactions between synaptic partners (Cohen-Cory, 2002; Vaughn et al., 1974; Ziv and Smith, 1996). However, little is known about the role of stochastic filopodial dynamics for robust synapse formation.

Presynaptic active zone assembly is a key step in synapse formation and regulated by a conserved set of proteins (Owald and Sigrist, 2009; Schoch and Gundelfinger, 2006). An early active zone "seeding" step has been defined through the functions of the multidomain scaffold proteins Syd-1 and Liprin-α in *C. elegans* and *Drosophila* neuromuscular junction (NMJ) (Dai et al., 2006; Owald et al., 2010). Syd-1 is a RhoGAP-domain-containing protein (Hallam et al., 2002) that recruits Liprin-α to the active zone (Owald et al., 2010). Liprin-α is an adaptor protein named after its direct interaction with the receptor tyrosine phosphatase Leukocyte common antigen-related (LAR) (Serra-Pagès et al., 1995; Zhen and Jin, 1999). The Liprin-α and LAR interaction has been directly implicated in active zone assembly across species (Dunah et al., 2005; Kaufmann et al., 2002). Downstream, Liprin-α and Syd-1 recruit core active zone components and ELKS/CAST family protein Brp (Dai et al., 2006; Fouquet et al., 2009; Wang et al., 2002). Finally, the RhoGEF Trio has been proposed to function downstream of the Lar/Liprin-α/Syd-1 (Astigarraga et al., 2010; Debant et al., 1996; Holbrook et al., 2012) and has recently been suggested to regulate active zone size (Spinner et al., 2018).

Remarkably, the proposed Lar-Liprin-α-Syd-1-Trio pathway has been characterized in parallel for its role in axon guidance, independent of active zone assembly (Bateman et al., 2000; Wills et al., 1999; Xu et al., 2015). In the *Drosophila* visual system, mutants in all four genes have been implicated in the layer-specific targeting of photoreceptor R7 axons in the medulla neuropil (Choe et al., 2006; Clandinin et al., 2001; Hofmeyer et al., 2006; Holbrook et al., 2012; Maurel-Zaffran et al., 2001; Newsome et al., 2000b). It is unclear whether any of the four mutants affect active zone assembly in R7 neurons. Dual roles in axon pathfinding and synapse formation have been shown or proposed for all four genes (Astigarraga et al., 2010; Hakeda-Suzuki et al., 2017; Holbrook et al., 2012; Maurel-Zaffran et al., 2001; Weng et al., 2011). Independent

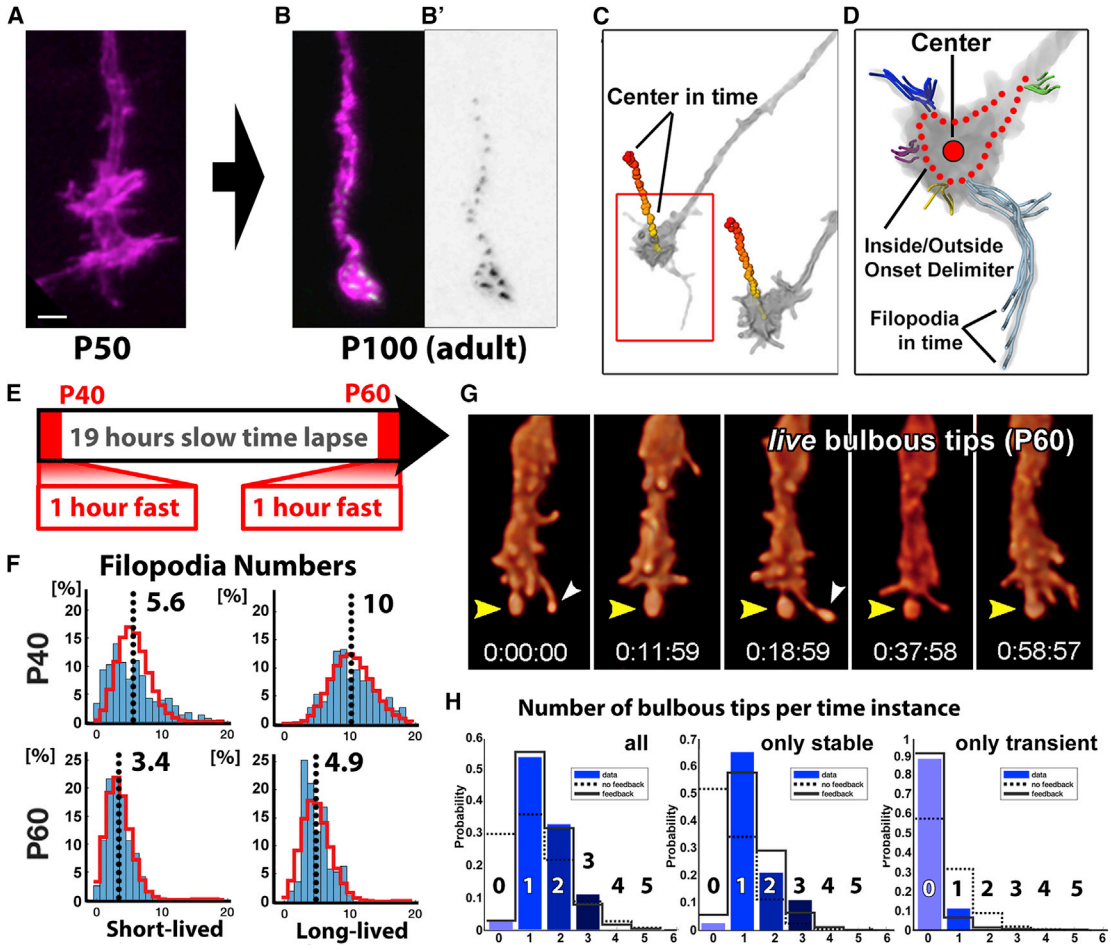

Figure 1. 4D Filopodia Tracking Reveals Stochastic Dynamics Prior to Synapse Formation and Rare "Bulbous" Filopodia that Stabilize One at a Time during Synapse Formation

(A) *Drosophila* R7 photoreceptor axon terminals transition from a growth cone-like structure with multiple filopodia just prior to synapse formation at 50% pupal development (P50) to a smooth, adult terminal.

(B) The adult R7 terminal has 20–25 synapses and no filopodia (magenta, CD4-tdTomato; green, BrpD3-GFP).

(C) A semi-automatic method for 4D filopodia tracking is based on tracking growth cone centers.

(D) Semi-automatic tracking of filopodia with the Amira filament editor.

(E) Imaging protocol for >20 h continuous time lapse and fast imaging at P40 and P60 for the same axon terminals.

(F) R7 filopodia fall into short-lived and long-lived classes that both fit Poisson (stochastic) distributions at both P40 and P60.

(G) Representative snapshots of an R7 axon terminal in the brain at P60 with a continuous stable bulb (yellow arrowhead).

(H) Number of bulbous filopodia at P60. Separation into stable (middle) and transient (right) bulbs reveals that most time points contain 1–2 stable bulbs. The distributions can be fit with negative feedback (sold black lines) but not with Poisson product distributions (dotted lines). Scale bar, 2 μm.

implications in active zone assembly and axon pathfinding raise the question what functions are primary or secondary.

In this study, we investigated the relationship between filopodial dynamics and synapse assembly in the presynaptic R7 terminal. The early synaptic seeding factors Liprin-α and Syd-1 accumulate in only a single filopodium per terminal at any given point in time. Consequently, only 1–2 filopodia per terminal are stabilized, suggesting that only 1–2 filopodia are synaptogenic at any time. A data-driven computational model shows that this "serial synapse formation model" is supported by the measured dynamics and could be tested in mutants for *liprin-α, syd-1*, *lar,* and *trio*. Specific defects in filopodial dynamics precede all other defects, including axon terminal retractions. We present a quantitative "winner-takes-all" model, from stochastic filopodial dynamics to the formation of a limited number of synapses, as well as a model for axon terminal stabilization based on filopodia and synapses.

RESULTS

In each optic lobe, ~800 R7 axon terminals reach their adult morphology as column-restricted, smooth, and bouton-like structures that contain around 20–25 presynaptic release sites (Figures 1A and 1B) (Chen et al., 2014; Takemura et al., 2013). By contrast, during synapse formation these axon terminals exhibit highly dynamic filopodial extensions (Figure 1A). The role of R7 filopodial dynamics in the second half of pupal development (P + 50%–100%) is unknown.

4D Filopodia Tracking Reveals Stochastic Dynamics Prior to Synapse Formation and Rare "Bulbous" Filopodia during Synapse Formation

The characterization of axon filopodia dynamics during synapse formation in the intact brain required a method to obtain quantitative high-resolution, long-term 4D data throughout the second half of fly brain development. We had previously developed a long-term culture of intact developing brains in an imaging chamber (Özel et al., 2015), but the challenge of tracking fast dynamics for thousands of filopodia in a developing brain have so far precluded large-scale analyses. We therefore devised a semi-automatic method for quantitative filopodia tracking based on a previously developed "filament editor" (Figures S1A and S1B) (Dercksen et al., 2014). In short, the algorithm predicts the growth cone centers for all time points by similarity-based propagation from the initial time point and thereby streamlines the segmentation of individual terminals (Figure 1C). Next, filopodia are traced at each time point, sequentially propagated, and automatically matched to the corresponding filopodia at other time points based on the vicinity of their starting points (Figure 1D). Using this method, we tracked 27,390 individual filopodia through time and space across 38 growth cones (STAR Methods; Figures S1A and S1B).

We first analyzed wild-type R7 axon development from just before synapse formation (P + 40%, P40) until after 20–22 h in culture, during synapse formation (P + 60%, P60) for the same growth cones (1 min time lapse for 1 h periods; Figure 1E). 4D tracking of several thousand filopodia revealed two distinct classes with separate exponential lifetime distributions: transient filopodia with a maximum lifetime of 8 min (short-lived), and stable filopodia with lifetimes of more than 8 min (long-lived) (Figure S1C) with similar length and velocity distributions (Figure S1D). At any time point at P40 each R7 terminal has twice as many long-lived (>8 min) compared to short-lived (<8 min) filopodia (Figure 1F). The numbers of both classes reduce significantly by P60 (Figure 1F), and by P100, all filopodia disappear (Figure 1B). The measured filopodia exhibit linear stochastic dynamics, since all four distributions (long- and short-lived filopodia at P40 and P60) almost perfectly fit Poisson distributions (Gadgil et al., 2005) (red traces in Figure 1F; STAR Methods, Mathematical Modeling).

In addition to the great majority of transient filopodia, we also consistently observed rare, long-lived filopodia that develop characteristic "bulbous tips" around the time of synapse formation (Özel et al., 2015). Quantitative analyses revealed no bulbous tips prior to synapse formation at P40. In contrast, at P60 there are 1–2 stabilized filopodia with bulbous tips present at any time point, most of which have a lifetime of >40 min (Figures 1G and 1H; Video S1). Because many of these bulbous filopodia existed before and after the 1 h imaging window, the lifetime estimate is certainly an underestimation, and we observed bulbous tips that existed for hours in long-term time lapse. Notably, we counted almost no time instances with 0 bulbs (Figures 1G and 1H; Video S1). This heavily right-skewed distribution is indicative of a regulatory mechanism: while the absence of regulatory mechanisms would give rise to a Poisson product distribution (dotted lines in Figure 1H), the inclusion of an inhibitory feedback, whereby existing bulbs suppress new bulbs, reveals an excellent fit of the observed distribution (solid lines in Figure 1H). This skewed distribution causes a bulbous tip to be present at almost every time point, while a Poisson product distribution (= no feedback) would result in many time points without bulbs. Correspondingly, almost 100% of time points have at least one bulb but rarely more than two. Hence, at the time of synapse formation, R7 growth cones continuously stabilize only 1–2 filopodia at any time point, while the overall number of filopodia decreases continuously from P40 until adulthood.

Only 1–2 Filopodia at Any Time Point Accumulate Synaptic Seeding Factors

Competitive stabilization of only 1–2 filopodia could be achieved through a "winner-takes-all" mechanism of filopodial competition. We asked whether synaptic building proteins would exhibit such a competitive distribution at filopodial tips. First, we tested whether the active zone protein Bruchpilot (Brp) is associated with filopodia. Fluorescently tagged BrpD3 (or Brp^{short}) is a reliable marker for mature synapses and localizes specifically to sites of intrinsic Brp without affecting synapse function or causing overexpression artifacts (Berger-Müller et al., 2013; Schmid et al., 2008; Sugie et al., 2015). We never found BrpD3-marked mature active zones in filopodia, similar to recent findings in developing adult motoneurons (Constance et al., 2018) (Figures 2A, 2B, and 2G). To measure the dynamics of synapse formation, we performed live imaging of BrpD3 at 10 min resolution over several hours around P + 70% (P70) (Video S2). BrpD3 is strikingly excluded from filopodia; puncta never move into or form in filopodial tips, and instead form by gradual accumulation on the axon terminal main body. Tracking individual puncta for over 5 h revealed that the vast majority of BrpD3-positive synapses are stable once formed (Figure 2H; Video S2). We conclude that mature synapses marked by BrpD3 are not associated with filopodia but only form on the axonal trunk where they are stable once formed.

At the *Drosophila* neuromuscular junction, Brp is recruited late to nascent synapses by the early seeding factors Syd-1 and Liprin-α (Owald et al., 2010). We overexpressed GFP-tagged variants of each protein and asked to what extent they localize to filopodia. Unlike BrpD3-GFP, GFP-tagged Liprin-α and Syd-1 occur in bulbous filopodia tips (Figures 2C–2G). Remarkably, clearly discernable accumulations of Liprin-α and Syd-1 are only apparent in one or sometimes two bulbous filopodia, while the majority of filopodia contain no signal (Figures 2C–2G). In contrast to other filopodia, the number of filopodia tips containing Syd-1 or Liprin-α does not decrease between P50 and P70 but remains constant at 1–2 per axon terminal. Note that most filopodia do not contain any detectable Syd-1 or Liprin-α despite large amounts of overexpressed proteins in the axon terminal trunks. The 1–2 positive filopodia could not be predicted based on size or length of the filopodia (compare c′–f′ to c″–f″). Antibody labeling of Syd-1 in the wild type compared to *syd-1* mutant R7 axon terminals confirmed the same sparse distribution to bulbous filopodia for the endogenous protein (Figures S2A–S2C). Our findings support the idea that Syd-1 and Liprin-α match the criteria for a "winner-takes-all" distribution: both localize sparsely and non-randomly to 1–2 filopodia per axon terminus.

Live imaging revealed the localization of Liprin-α-GFP only to stable filopodia with bulbous tips, while dynamically moving in

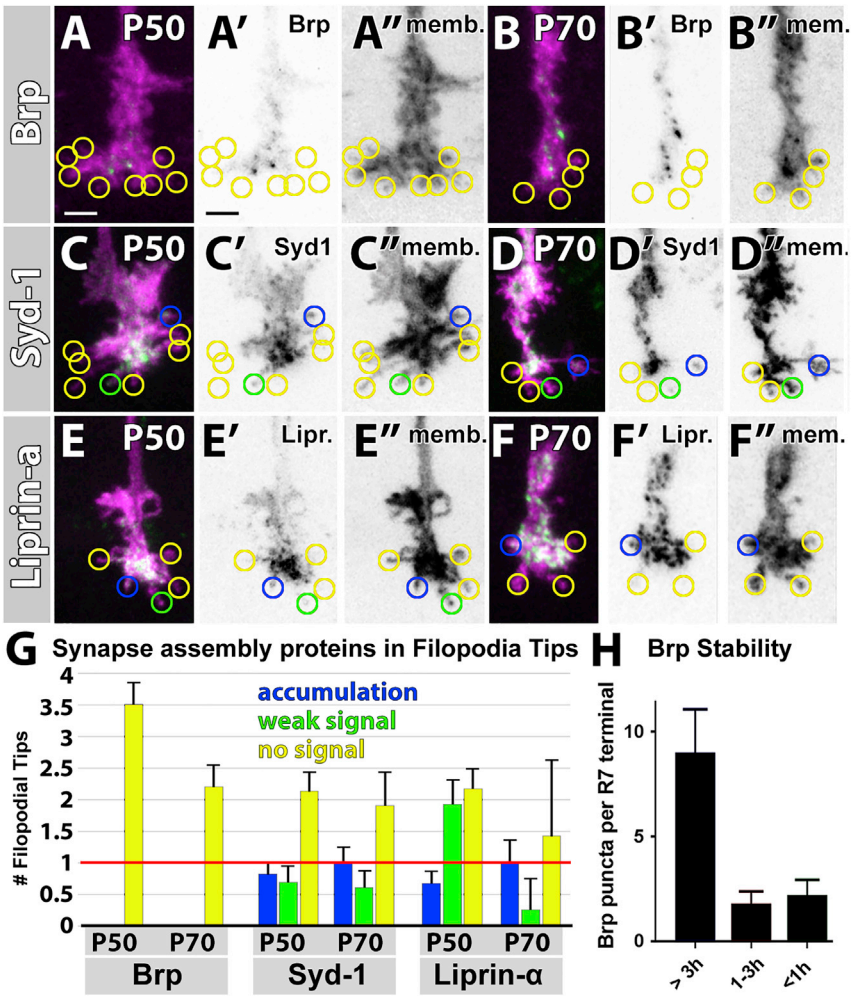

Figure 2. One Filopodium at a Time Accumulates Synaptic Seeding Factors

(A–F) Localization in R7 photoreceptor terminals and filopodia for BrpD3-GFP at P50 (A) and at P70 (B), GFP-Syd-1 at P50 (C) and at P70 (D), and Liprin-α-GFP at P50 (E) and at P70 (F). Yellow circles indicate filopodia with no measurable GFP signal, green circles weak signal, and blue circles clear accumulations. (A′–F′) show the single channel for the GFP-tagged proteins (green), and (A″–F″) show the single channel for the membrane tag CD4-tdTomato (magenta). Scale bar, 2 μm.

(G) Quantification of filopodial accumulation of the three proteins.

(H) Number of BrpD3 punctae per R7 terminal binned according to their lifetimes. R7 terminals were live imaged at 10 min resolution starting at P + 50% + 22 h in culture. Individual punctae were tracked for 5.5 h to determine lifetimes (n = 5 terminals). Error bars denote SEM.

and out of filopodia (Video S3); GFP-Syd1 puncta were too dense for reliable tracking, but similar to Liprin-α, only exhibit clear accumulations in 1–2 bulbous filopodia per axon terminal at all times. These observations suggest that synapse assembly may start in filopodia. The data are further consistent with reversible molecular "seeding" events (Owald et al., 2010) and filopodia stabilization through nascent synapses, as previously observed (Constance et al., 2018; Meyer and Smith, 2006). The findings suggest a model whereby only 1–2 filopodia at a time may be synaptogenic, i.e., competent to form a synapse.

A Data-Driven Computational Model Predicts "Serial Synapse Formation" Based on Competition and Negative Feedback of Bulbous Filopodia

We tested a series of Markov models of filopodia dynamics based on the measured data at P40 and P60 before arriving at a model consistent with all observations (Figure 3A; see also STAR Methods, Mathematical Modeling). We first modeled suppression of filopodia by synapses, such that the increasing number of synapses over time would lead to a decreased production of filopodia, until all filopodia are gone by P100 and a specific number of synapses have been generated. However, this model did not explain the non-Poisson distribution of bulbous filopodia seen in Figure 1H (see Mathematical Modeling in STAR Methods). By contrast, suppression of new bulb generation through feedback by the bulbous filopodia themselves provided a minimal model that explains the non-Poisson distribution of bulbous filopodia as well as the slow progression of synapse formation (Figure 3A). The model recapitulates the birth of filopodia, their transitions between short-lived and long-lived filopodia, transitions to bulbous filopodia, and finally transitions to synapses (Figures 3A, 3C, 3E, and 3G).

The live-imaging data provide direct measurements of the filopodial birth and death rates (r1 and r2) and the observed rates of bulb disappearance (r4) (all measured data are labeled in blue in Figure 3). Because of the introduction of inhibitory feedback on bulb formation, the average rate of bulb initiation (r3) at P60 is the product of a propensity to form bulbs (r2B) and the average inhibitory feedback f1, such that absence of feedback (f1 = 1) represents no inhibition of r3 and maximal negative feedback (f1 = 0) represents complete inhibition of r3. Based on the measurement of bulb appearances and the observed right-skewed distribution of bulbs (Figure 1H), we determined the exclusive set of r2B and f1 that fit the observations for time point P60 (Table S1). Negative feedback f1 in WT is close to maximal, which ensures the measured sharp distribution of only 1–2 bulbs per time instance with almost no time instance of zero bulbs. As shown in Figure 1H, almost every transient bulb stabilizes (r5). Lastly, we estimated the rate of synapse formation (r6) from the maximal slope in Figure 3F. The number of mature synapses matched previous measurements (Chen et al., 2014; Takemura et al., 2013).

In addition to the live dynamics measurements at P60, we counted total numbers of filopodia, bulbous tips and synapses (BrpD3) in fixed preparations for the time points P40, P50, P60, P70, P80, P90 and P100 (blue data points in Figures 3B, 3D,

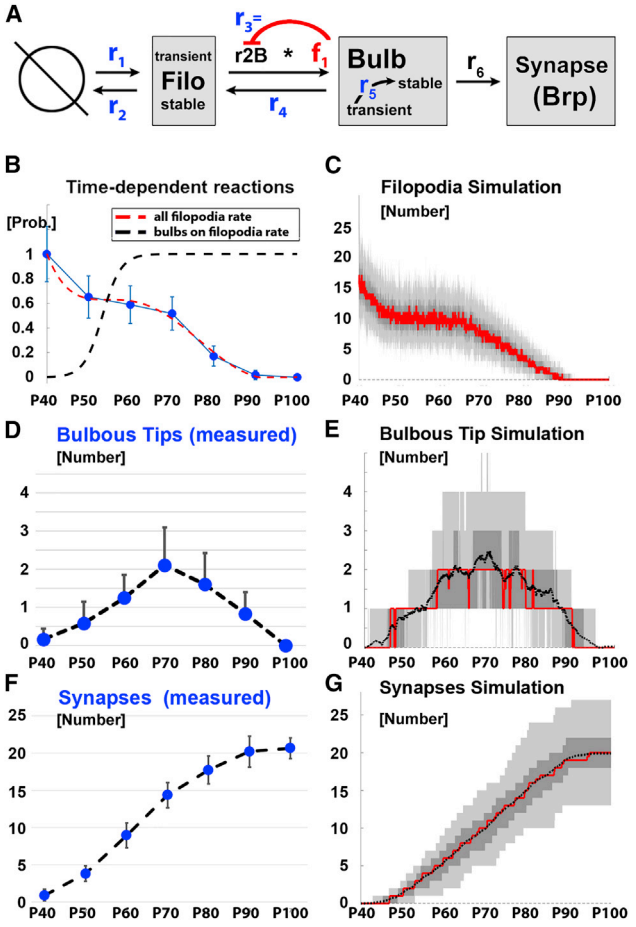

Figure 3. A Data-Driven Computational Model Predicts "Serial Synapse Formation" Based on Competition and Negative Feedback of Bulbous Filopodia

(A) Summary of the data-driven Markov state model from filopodial birth to synapse formation. All rates in blue are measured from live-imaging data. Rates r_1 and r_2 denote the generation and retraction of filopodia; r_3 and r_4 denote the formation and degeneration of a bulbous tip; r_5 denotes the stabilization of the bulbous tip and r_6 the formation of a synapse.

(B) Estimation of time-dependent function required for the modeling from P40–P100 (40%–100% of pupal development). The reduction of filopodia was based on measured filopodial counts from fixed preparations (blue disks = average, error bars = standard deviation) and modeled by a time-dependent function $f_F(t)$ (dashed red line) as outlined in the STAR Methods. The increased propensity to form bulbs on these filopodia (black dashed line) was estimated based on bulb measurements shown in (D) and as explained in the STAR Methods.

(C) Output of Markov state model for filopodial dynamics based on measured rates according to the model in (A). Solid red lines indicate the *median* number of bulbs from the stochastic simulations, whereas dark gray areas denote the interquartile range (50% of the data) and light gray, the 95% confidence range from the simulations.

(D) Measured number of bulbous tips (disks = average, error bars = standard deviation).

(E) Output of Markov state model for the development of bulbous tips. Black dotted lines: *average* number of bulbs; solid red line: *median* number of bulbs; gray confidence ranges as in (C).

(F) Measured numbers of synapses between P40 and P100 (disks = average, error bars = standard deviation).

(G) Output of Markov state model for synapse formation. Black dotted lines: *average* number of bulbs; solid red line: *median* number of bulbs; gray confidence ranges as in (C).

and 3F). The live P60 data match the fixed counts at P60 well. Based on these data, we determined a function for the filopodial decline (red dotted line in Figure 3B) and the propensity to form bulbs (black dotted line in Figure 3B; see STAR Methods, Mathematical Modeling). Based on the measured data and these two rates, we modeled the changes to types (filopodia and bulbs) and numbers of filopodia over time in 3,600 time steps, equivalent to 3,600 min from P40 to P100. The resulting model reproduces a minute-by-minute simulation of the number of filopodia (Figure 3C), bulbs (Figure 3E), and synapses (Figure 3G). For model building and parameter estimation based on the measured data, see STAR Methods section on Mathematical Modeling.

The appearance of only 1–2 bulbous tips at any time point between P55 and P85 leads to a continuous, limited generation of mature synapses that matches well with measured BrpD3 data (Figures 3F and 3G). Furthermore, the model predicts variability of synapse numbers similar to the measured variability. We conclude that our serial synapse formation model, based on measurements of filopodia and competitive feedback between bulbs, can in principle explain the kinetics and distribution of synapse development observed in the wild type.

Competition could either be the result of an active communication mechanism between filopodia, or, alternatively, passively arise from the uneven distribution of a limiting amount of synaptic seeding factors. We considered the restrictive distribution of seeding factors as a basis to model them as a resource with limited access to filopodia. In this model, a competitive advantage occurs if the accumulation of seeding factors is associated with increased filopodial lifetime, which in turn provides more time for further accumulation of seeding factors, which further increase lifetime. Our modeling shows that for a limited amount of synaptic seeding factors available to filopodia, such a "runaway" positive feedback loop can lead to the accumulation of the majority of available seeding factors in just 1–2 bulbous filopodia (STAR Methods; Figures S3 and S4. A passive mechanism can thereby effectively prevent other filopodia from accumulating enough seeding factors to stabilize. Hence, "winner-takes-all" dynamics can arise from the dynamic distribution of a limited resource that confers a competitive advantage without the need for active filopodial communication or additional competitive mechanisms.

Loss of Synaptic Seeding Factors Syd-1 and Liprin-α Causes a Loss of Inhibitory Feedback during Filopodial Bulb Formation

Since our model predicts a role for synapse formation molecules in bulb stabilization, we tested the model experimentally in mutants. First, we tested the consequences of a loss of *brp* during R7 axonal development with a previously tested combination of two RNAi constructs (Wagh et al., 2006) and confirmed the known defect in neurotransmission (Figures S5A and S5B). The knockdown of *brp* has no effect on the transition of R7 terminal morphology from filopodial to smooth bouton-like structures (Figure S5C). These findings indicate no role for Brp in axon terminal development and are consistent with the absence of Brp from filopodia (Figure 2). These findings further resemble previous observations in motoneurons (Constance et al., 2018) and are consistent with the observation of normal development in the absence of neurotransmission (Hiesinger et al., 2006).

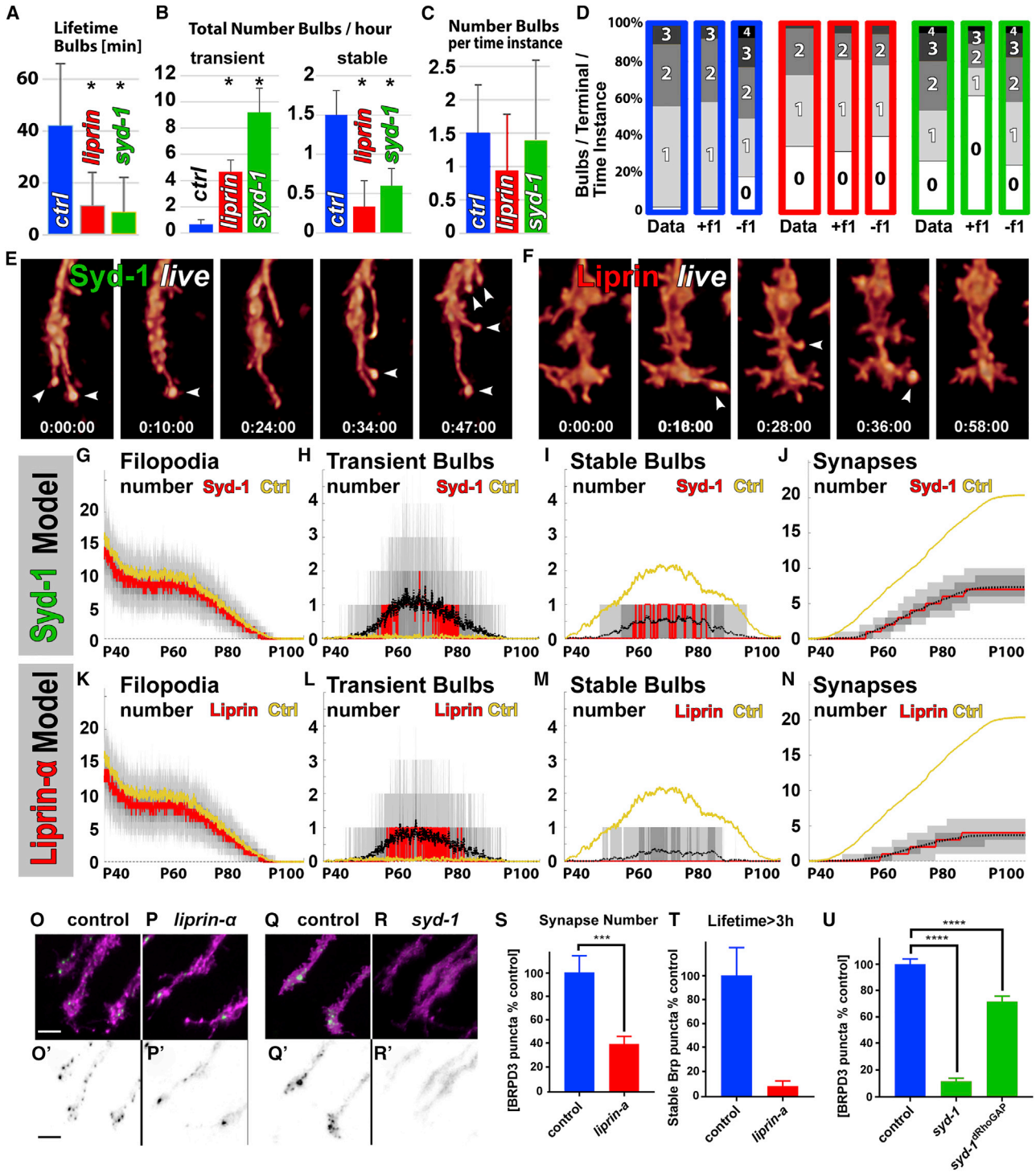

Figure 4. Loss of Synaptic Seeding Factors Syd-1 and Liprin-α Causes a Loss of Inhibitory Feedback and Filopodial Bulb Destabilization

Analyses of Filopodial Dynamics and Synapse Formation for *syd-1* (Green), *liprin-α* (Red), and Control (Blue)

(A) Lifetime of bulbous filopodia.

(B) Total number of bulbous filopodia per terminal per hour.

(C) Average number of bulbous filopodia per time instance.

(D) Number of concurrently existing bulbous filopodia per axon terminal per time instance observed in the data, simulated after inclusion of a feedback (+f1) and without a feedback (−f1).

(E and F) Representative snapshots of *syd-1* (E) and *liprin-α* (F) revealing only transient bulbs.

(legend continued on next page)

To perturb early stages of synapse formation, we investigated mutants for *liprin-α* and *syd-1*. The analysis of filopodial dynamics is complicated by previous observations of R7 axon targeting defects for both mutants (Choe et al., 2006; Hofmeyer et al., 2006; Holbrook et al., 2012). To characterize the timeline and origin of these defects, we performed long-term live imaging from P + 30%–P + 70% for single mutant, positively labeled R7 cells in an otherwise heterozygous background (MARCM) (Lee and Luo, 1999). Our analyses of both mutants (*liprin-α*^{E} (Choe et al., 2006), *syd-1*^{w46} (Holbrook et al., 2012)) revealed that all mutant R7 axons initially target correctly. Axon terminal dynamics of both *liprin-α* and *syd-1* mutant axons are indistinguishable from the wild type until P40 (Figures S6A–S6C). Starting around P50, i.e., during the time period of synapse formation, individual terminals retract. At P60, the majority of *liprin-α* or *syd-1* mutant R7 axon terminals continue to remain in their correct target layer. We therefore first performed a quantitative analysis of filopodial dynamics at P40 and P60 for those terminals that remained stable in their correct target layer. We provide a detailed analysis of retraction events in the last section (Figure 6).

Quantitative 4D tracking of filopodia of both *liprin-α* or *syd-1* mutant R7 axon terminals at P40 and P60 revealed distributions of numbers, lifetimes, lengths and velocities that are largely indistinguishable from the wild type (Figures S6A–S6O). *syd-1* mutant axon terminals exhibit individual, unusually elongated filopodia during synapse formation, but their low number does not affect the statistics significantly (Figure S6M). In contrast to other filopodia, the dynamics of bulbs were significantly altered. The lifetimes of bulbs in both *syd-1* and *liprin-α* were reduced by 70%–80% (Figure 4A). Bulb destabilization is also reflected in a similar ~70% decrease in the number of stable (>40 min) bulbous filopodia in both mutants. Correspondingly, the number of short-lived, destabilized bulbs is dramatically increased by 10- to 20-fold (Figure 4B; Video S4). The reduced lifetimes and increased numbers are a result of increased rates for both bulb appearance (r3) and bulb disappearance (r4) as measured at P60 (Table S1). A remarkable consequence of corresponding increases in both bulb generation and destabilization is that the average number of bulbs observed per time instance, i.e., the average appearance of what a fixed image would look like, is not significantly different from the wild type (Figure 4C). These findings suggest that the absence of synaptic seeding factors leads to a defect in bulb stabilization, resulting in continuous attempts to form new bulbs. Bulb stabilization by synaptic seeding factors is consistent with a competitive, non-random distribution of Liprin-α and Syd-1 proteins to filopodia. We conclude that synaptic seeding factors are required for bulb stabilization but not for bulb initiation.

Next, we analyzed the distribution of bulbs present at any given time point over a 1 h period at P60. In contrast to the wild type, both *syd-1* and *liprin-α* exhibit 20%–30% of all time points without any bulbs (Figure 4D). In the wild type, the bulb distribution (blue boxes, data as in Figure 1H) does not match a Poisson distribution without feedback (−f0) but can be simulated with inhibitory feedback (+f1) as described for Figure 1H. By contrast, both *syd-1* and *liprin-α* (green and red boxes, respectively) resemble Poisson product distributions (−f0) and are not better matched by applying the inhibitory feedback (+f1) (Figure 4D, note that smaller f1 values indicates stronger feedback in Table S1). As with the wild-type data, the observed rate of bulb appearance (r3) could be fitted with a single product of the average propensity to form a bulb (r2B) and the average inhibitory feedback (f1) at P60 (Figure 3A). In both mutants the feedback is mostly lost (f1 > 10-fold increased; Table S1). Together with a reduced bulb stabilization rate r5 in both mutants, the loss of feedback results in a high frequency of transient bulbs for both *syd-1* (Figure 4E; Video S4) and *liprin-α* (Figure 4F; Video S4).

We next simulated the entire time course from P40 to P100, from filopodial dynamics to synapse formation as established for the wild type (Figure 3), using the measured live data at P60 for each mutant. For *syd-1*, overall filopodia numbers are slightly below the wild type (Figure 4G). However, in contrast to the wild type, the simulation recapitulates the formation of large numbers of transient bulbs (Figure 4H) but very few stabilized bulbs (Figure 4I). In contrast, the wild type forms almost no transient bulbs because all bulbs stabilize (compare black trace for mean in *syd-1* to yellow traces of the mean for control in Figures 4H and 4I). The *liprin-α* simulation revealed a similar increase of transient bulbs combined with a further reduced number of stable bulbs (Figures 4K and 4M). As a result of this altered distribution, the simulation predicts a reduction of adult synapses in *syd-1* and *liprin-α* to 35% and 20% of the wild-type levels, respectively (Figures 4J and 4N). These simulated reductions occur without changes to the synapse formation rate r6 and are purely because of the observed defect in bulb stabilization; an additional direct effect of *syd-1* or *liprin-α* on synapse formation itself, as has been argued based on their molecular function as synaptic seeding factors (Owald et al., 2010), would reduce the number of synapses further.

To assess the number of synapses *in vivo* we performed BrpD3 counts at P70 in R7 axon terminals in their correct target layer. The number of BrpD3-positive synapses is significantly reduced in *liprin-α* (Figures 4O, 4P, and 4S) and almost completely abolished when a 3 h stability criterion is applied (Video S5; Figure 4T). Similarly, *syd-1* mutants exhibit almost no BrpD3-positive synapses (Figures 4Q and 4R). We also generated a precise CRISPR-mediated knockin of a mutant version of *syd-1* lacking putative RhoGAP activity, which was previously predicted to play a role in active zone assembly

(G–N) Markov state model simulation for *syd-1* and *liprin-α*. (G) filopodia number for *syd-1* and control; (H) transient bulbs number for *syd-1* and control; (I) stable bulbs number for *syd-1* and control; (J) synapses number for *syd-1* and control; (K) filopodia number for *liprin-α* and control; (L) transient bulbs number for *liprin-α* and control; (M) stable bulbs number for *liprin-α* and control; (N) synapses number for *liprin-α* and control. In all cases, control traces from Figure 3 are shown in yellow. Black dotted lines, mean number of bulbs; solid red line, median number of bulbs; dark gray denotes the interquartile range (50% of the data); and light gray, the 95% confidence range.

(O–R) Measurement of BrpD3 punctae in mutant axon terminals. (O) control; (P) liprin-α; (Q) control; (R) syd-1.

(O′–R′) BrpD3 single channel. Scale bar, 2 μm.

(S) Quantification of BrpD3 synapse numbers per terminal relative to control. n = 18 and 16 (p = 0.0007). (T) Number of BrpD3 punctae per terminal with lifetimes greater than 3 h in R7 axons live imaged for 4 h at P + 70% in the wild type (n = 5) and *liprin-α*^{E} mutants (n = 5).

(U) Quantification of synapse numbers in *syd-1*$^{\Delta RhoGAP}$ flies. n = 45, 18, and 32 (p < 0.0001). Error bars denote SEM.

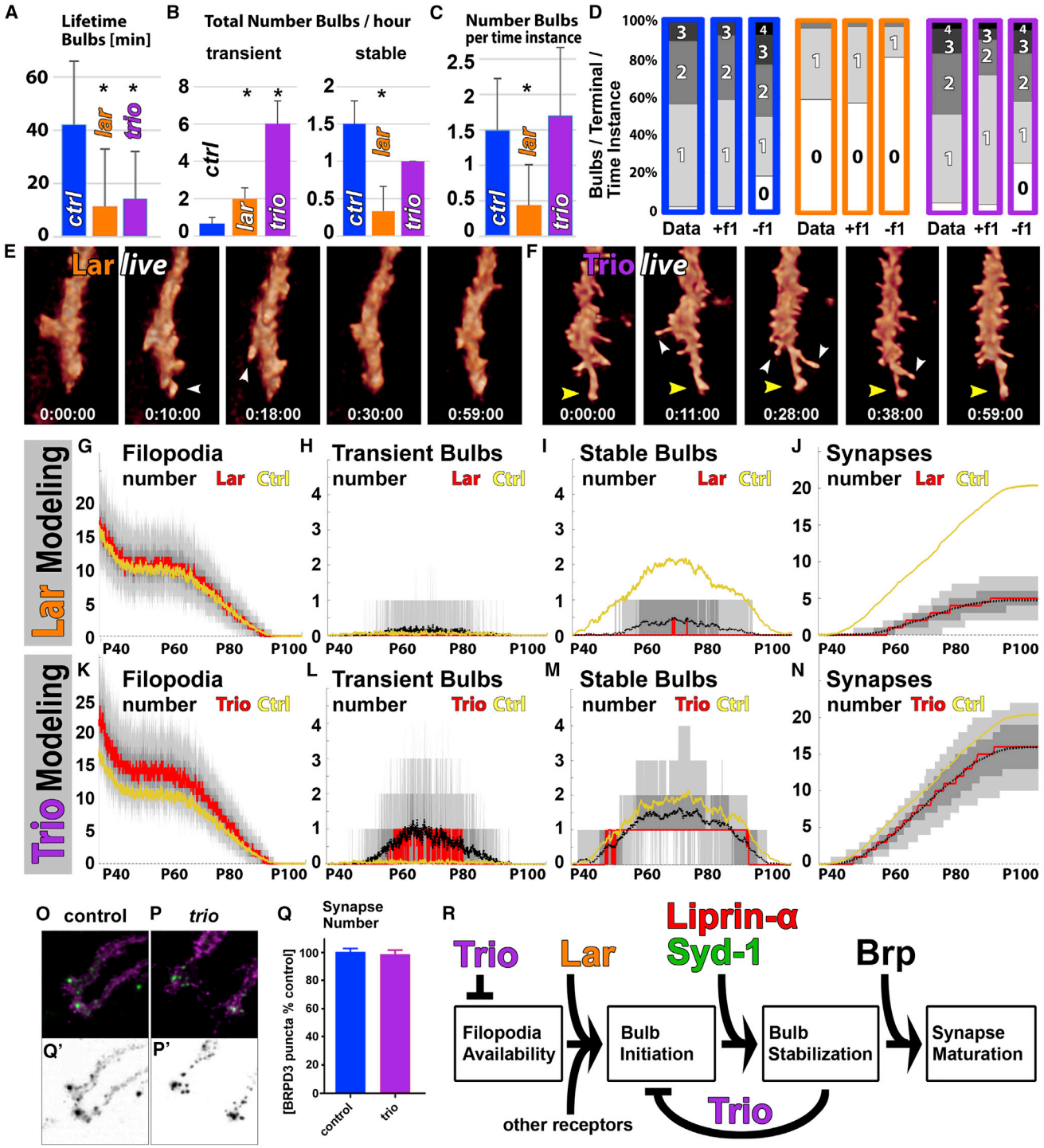

Figure 5. Analysis of the Syd-1-Liprin-α Pathway Components Reveal a Role for Lar, but Not Trio, in Bulb Initiation Analyses of Filopodial Dynamics and Synapse Formation for *lar* (Orange), *trio* (Magenta), and Control (Blue)

(A) Lifetime of bulbous filopodia.

(B) Total number of bulbous filopodia per terminal per hour.

(C) Average number of bulbous filopodia per time instance.

(D) Number of concurrently existing bulbous filopodia per axon terminal per time instance observed in the data, simulated after inclusion of a feedback (+f1) and without a feedback (−f1).

(E and F) Representative snapshots of *lar* (E) and *trio* (F) revealing only transient bulbs.

(legend continued on next page)

(Wentzel et al., 2013; Spinner et al., 2018). This gene-edited allele fully replaces the wild-type gene locus (Figures S5D and S5F). However, in contrast to loss of *syd-1*, the *syd-1*$^{\Delta RhoGAP}$ mutant flies are viable and fertile and exhibit no obvious defects other than a relatively mild reduction of BrpD3-positive synapse numbers (Figures 4U and S5F–S5H) and are not further analyzed here. Consistent with studies in other systems, these findings indicate that *syd-1* and *liprin-α* are required for normal synapse formation also in R7. In sum, our findings support the hypothesis that both proteins function as a limiting resource for synaptic "seeding," which is in turn required for the stabilization of synaptogenic filopodia.

Analyses of Additional Pathway Components Reveal a Role for Lar, but Not Trio, in Bulb Initiation

The membrane receptor LAR and the RhoGEF Trio have been proposed to function in a pathway with Liprin-α and Syd-1 in the contexts of axon pathfinding and synapse formation (Astigarraga et al., 2010; Holbrook et al., 2012; Maurel-Zaffran et al., 2001; Weng et al., 2011). We therefore performed live imaging, filopodia tracking, and computational modeling for *lar* and *trio* mutant R7 axons analogous to WT, *syd-1*, and *liprin-α*.

Long-term live imaging of single mutant R7 axons showed that, similar to *liprin-α* and *syd-1*, both *lar* and *trio* axon terminals initially target correctly and exhibit no significant alterations of their filopodial dynamics prior to P40 (Figures S7A–S7C). However, individual *lar* mutant axon terminals exhibit the first probabilistic retractions shortly thereafter, resulting in retraction of nearly all terminals by P70, as previously reported (Clandinin et al., 2001; Maurel-Zaffran et al., 2001). In contrast, we did not observe any retractions of *trio* mutant axons. As with other mutants, we analyzed filopodial dynamics at P40 and P60 exclusively for axon terminals that remained stable in their correct target layer. We provide the detailed analysis of retractions in the last section (Figure 6).

Similar to *liprin-α* and *syd-1*, the dynamics of *lar* mutant R7 growth cones exhibit no significant differences of filopodia numbers, lifetimes, and lengths until P40 (Figures 7A–7C), except for a mildly increased birth rate r1 in *trio* (see model parameters in STAR Methods). Similarly, both short-lived and long-lived filopodia exhibit distributions for numbers and lengths that are similar to the wild type in both mutants at P40 and P60 (Figures S7D–S7O). Remarkably, bulb dynamics are the only significantly affected variable in both mutants. Similar to *syd-1* and *liprin-α*, both *lar* and *trio* mutants exhibit bulbs of significantly reduced lifetimes (Figure 5A; Video S6). Additionally, bulbs are destabilized in *lar* (Figure 5B). However, in contrast to *syd-1* and *liprin-α*, *lar* mutants form overall significantly less bulbs, suggesting a defect in bulb formation (Figure 5D) and a specific role for *lar* in the initiation of synaptogenic filopodia.

In contrast to lar, R7 axon terminals mutant for *trio* exhibit a strong increase of transient bulbs without significant loss of stable bulbs and a normal average number of bulbs per time instance (Figures 5B and 5C). These observations suggest that *trio* axon terminals can initiate and stabilize bulbous filopodia but form many additional unstable ones. Correspondingly, analysis of the bulb distribution at any given time point over a 1 h period at P60 separates *lar* and *trio* further from *syd-1* and *liprin-α*: In *lar*, the distribution is best matched with inhibitory feedback (+f1, orange boxes), suggesting partially intact feedback (Figure 5D; Table S1). In contrast, *trio* (magenta boxes) resembles the wild-type distribution (blue boxes, same control as Figure 4D), suggesting that in contrast to the other three mutants, one bulbous tip at any time point can still be stabilized (Figure 5D). This finding was further corroborated by live imaging (Video S6). Taken together, our mutant analyses suggest that *lar* is defective in bulb initiation (Figure 5E), lar, *syd-1*, and *liprin-α* fail to stabilize bulbs, and *trio* exhibits 1–2 stable bulbs plus supernumerary unstable bulbs (Figure 5F).

We next used our complete time course simulation from filopodial dynamics to synapse formation using the measured P60 data for *lar* and *trio*. As shown in Figure 5G, simulated *lar* mutant terminals form normal numbers of filopodia. In contrast to *syd-1* and *liprin-α*, very few transient or stable bulbs form in *lar* mutants (Figures 5H and 5I). Consequently, the *lar* simulation produces only very few synapses (Figure 5J). In contrast, *trio* exhibits continuously elevated levels of filopodia and increased number of transient bulbs (similar to *syd-1* and *liprin-α*) but also close to wild-type levels of stabilized bulbs (Figure 5M), which leads to close to wild-type levels of synapses (Figure 5N). Correspondingly, BrpD3 labeling reveals normal numbers of synapses in *trio* (Figures 5O and 5P). We could not reliably measure BrpD3-positive synapses in *lar*, because most axons are retracted by P70 and none retained a normal morphology. However, at P50, prior to Brp recruitment, Syd-1 still localizes to bulbous tips in *lar* mutant terminals, while Liprin-α is almost completely lost (Figures S2D–S2K. These findings suggest that the recruitment of Liprin-α, i.e. the Lar interacting protein α, depends on Lar. In contrast, in *trio* mutant terminals, both Syd-1 and Liprin-α exhibit unaltered localization to 1–2 bulbous tips at any time (Figures S2D–S2K). We conclude that the increased number of (unstable) bulbous filopodia in the *trio* mutant does not lead to increased numbers of synaptogenic filopodia, consistent with the measured numbers of synapses and the limiting resource model.

In summary, our data reveal largely normal axon targeting and filopodial dynamics until P40 for all mutants. *lar* exhibits defective bulb initiation and *lar*, *syd-1*, and *liprin-α* all fail to stabilize bulbs, leading to significant reductions in synapse formation. In contrast, in *trio*, "winner-takes-all" stabilization of 1–2 filopodia is intact, but selective negative feedback on further bulb initiation is defective. Hence, all four mutants fit distinct roles of the "winner-takes-all" mechanism and support the serial synapse formation model (Figures 5R and 7).

(G–N) Markov state model simulation for *lar* and *trio*. (G) filopodia number for *lar* and control; (H) transient bulbs number for *lar* and control; (I) stable bulbs number for *lar* and control; (J) synapses number for *lar* and control; (K) filopodia number for *trio* and control; (L) transient bulbs number for *trio* and control; (M) stable bulbs number for *trio* and control; (N) synapses number for *trio* and control. In all cases control traces from Figure 3 are shown in yellow. Black dotted lines, mean number of bulbs; solid red line, median number of bulbs; dark gray denotes the interquartile range (50% of the data); and light gray, the 95% confidence range. (O–R) Measurement of BrpD3 punctae in mutant axon terminals. (O) control; (P) trio. (O′–R′) BrpD3 single channel. Scale bar, 2 μm. (O–Q) Measurement of BrpD3 punctae in *trio* and control axon terminals. (O′–P′) BrpD3 single channel. (Q) Quantification of BrpD3-marked synapse numbers relative to control at P90. n = 87 and 61, p = 0.67 (R) Schematic summary of protein functions during synapse formation.

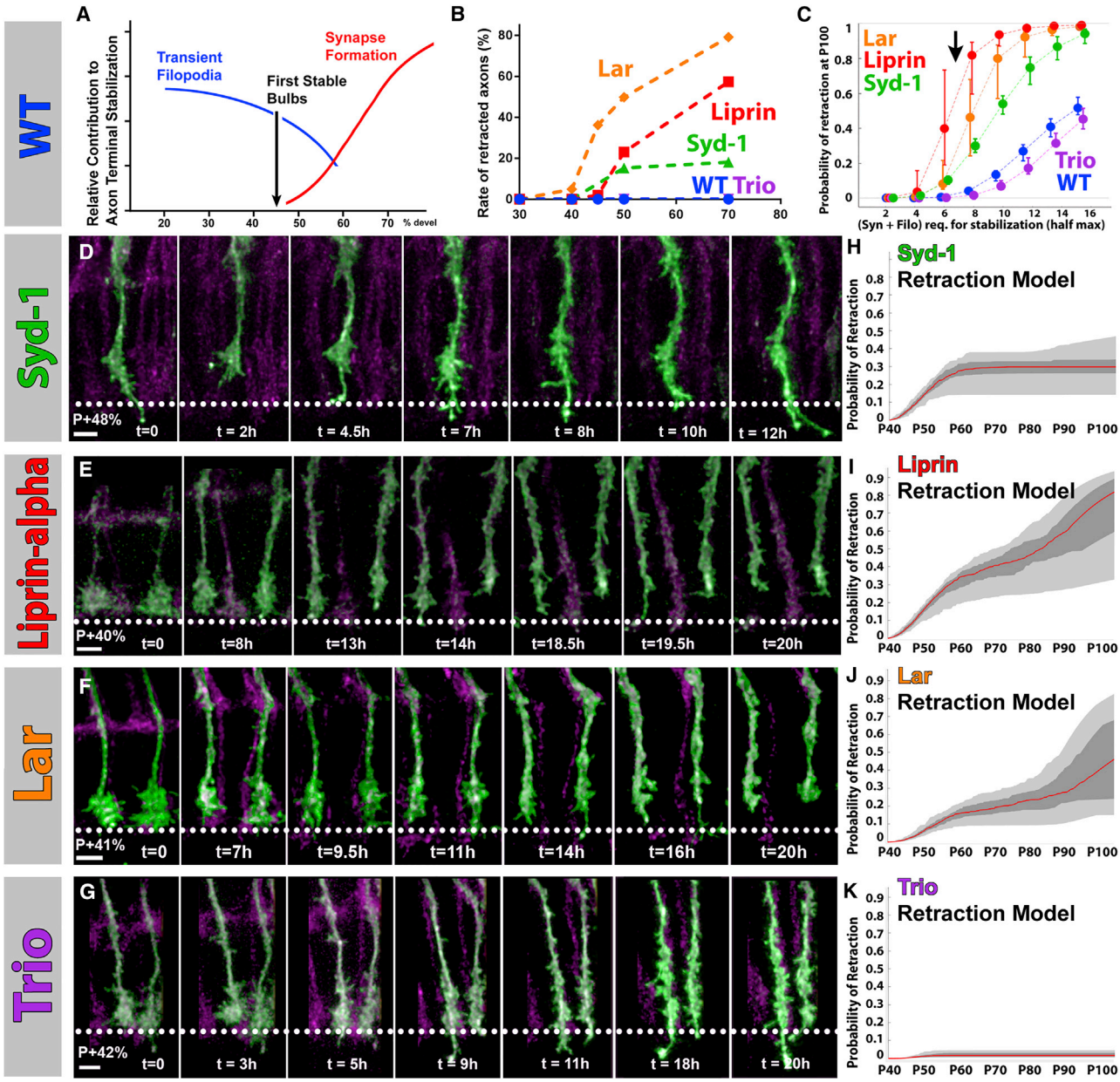

Figure 6. A Computational Model Predicts Axon Retractions in *lar*, *syd-1*, and *liprin-α*, but Not in *trio*

(A) Schematic of timeline during synapse formation, including continuous decline of transient filopodia, the first appearance of bulbs and the continuous increase in synapse numbers.

(B) Measured R7 axon retraction rates.

(C) Probability of R7 axon terminal retractions at P100 based on computational modeling of stabilization through a combination of transient filopodia and synapses.

(D–G) Representative time-lapse snapshots from long-term live imaging of R7 axon stabilization and retraction in the four mutants. (D) syd-1; (E) liprin-alpha; (F) lar; (G) trio. Dashed lines mark the wild-type R7 target layer (M6). Scale bars, 3 μm.

(H–K) Computational modeling of predicted probabilistic axon retractions between P40 and P100 for all four mutants (compare to measured data in B). (H) syd-1; (I) liprin-alpha; (J) lar; (K) trio. Solid red line, median; dark grey, interquartile range; light grey, 95% confidence range.

A Computational Model Predicts Axon Retractions in Mutants for *lar*, *syd-1*, and *Liprin-α*, but Not *Trio*

We have so far performed all analyses on normally targeted axon terminals that remained stable in the correct target layers, thereby isolating defects in filopodial dynamics and synapse formation independent of axon retraction. We therefore set out to test the idea that defective synapse formation might contribute to axonal destabilization. In contrast to *cadN* (Özel et al., 2015), none of the mutants analyzed here exhibited altered filopodial dynamics or retractions prior to P40, after which time synaptic partner identification is likely to start. The first stable bulbous filopodia can be observed around P45 and synapse formation increases thereafter (Figure 6A). Similar to filopodial adhesion, synapses may contribute to the stabilization of axon terminals. We therefore

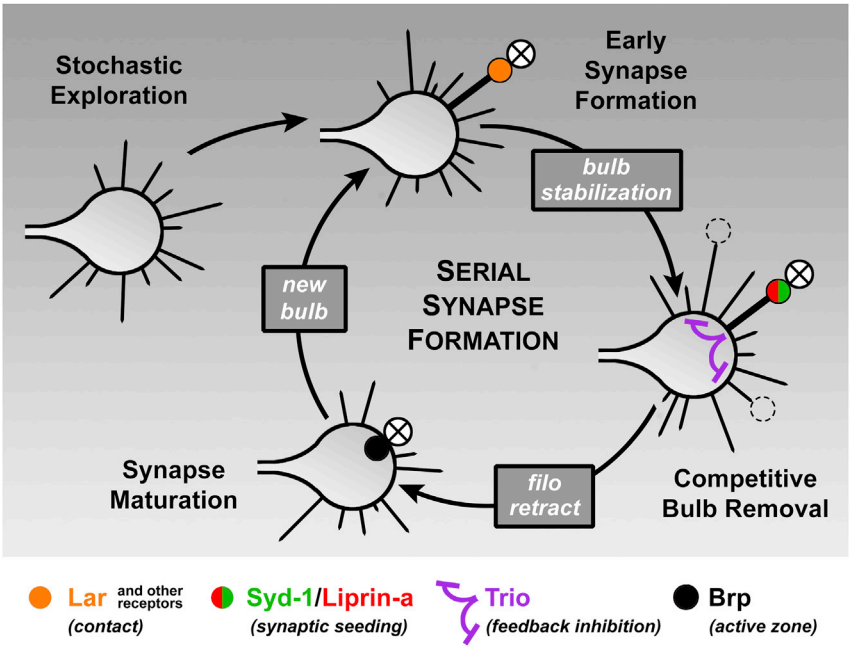

Figure 7. Serial Synapse Formation Model

The measured live dynamics and computational modeling suggest the following model: (1) stochastic filopodial exploration leads to synaptic capture via a cell surface receptor, e.g., Lar (2) early synaptic seeding factors (Syd-1 and Liprin-α) are recruited to the captured filopodium in an enlarged bulb; (3) secondary simultaneously forming bulbs are destabilized via the function of the RhoGEF Trio, thereby ensuring one synaptogenic filopodium at any given time; recruitment of the active zone protein Brp and synapse maturation occur after filopodial retraction back to the main axon terminal, allowing a new cycle of bulb formation and stabilization.

hypothesized that axon terminal stabilization may be a function of both filopodia and synapses (Figure 6A).

First, we measured the retraction rates between P40-P70 (Figure 6B). *lar* and *liprin-α* exhibit similar retraction rates with a 5-h delay for *liprin-α* after *lar*. The dynamics of these retractions appears similar in long-term live imaging of axon behaviors (Figures 6E and 6F; Video S7). In both cases, individual terminals probabilistically collapse to a smooth structure within 2 h and are not recognizably different just 1 h prior to collapse. A filopodial protrusion often remains for several hours, and the terminals retain the remarkable ability to re-extend to M6 but do not stabilize there. In contrast, apparent retraction of *syd-1* mutant axons plateau after P50 (Figure 6B); *syd-1* axons initiate retractions very similar to *liprin-α* and *lar* but exhibit many more re-extensions back to M6 and even beyond (Figure 6D; Video S7). This behavior contributes to the appearance of less retracted *syd-1* axons after P50 in fixed preparations (Figure 6B). *trio* mutant axons exhibit increased filopodial extensions that are somewhat similar to *syd-1*, explaining the earlier observations of an additional overextension phenotype in fixed preparations (Holbrook et al., 2012). We did not observe any retractions of *trio* mutant axons. However, careful analysis of *trio* mutant strains with the same genotypes as those used by Holbrook et al. (2012) revealed rare, misplaced R7 axons only in the original stocks from that study but not in different genetic backgrounds. Hence, *trio* may have a mildly increased probability to retract depending on the genetic background.

We next modeled retraction probabilities as a function of the number of filopodia and synapses. If only filopodia stabilize axon terminals, but not synapses, the model predicts similar retraction rates for wild type and all mutants (Figure S8). In contrast, if synapses contribute to axon stabilization, the different synapse formation rates of the four mutants differentially affect retractions. We tested the retraction probability as a function of an equally weighted sum of filopodia and synapses based on the measured filopodia and simulated synapse formation data for all four mutants. If very few filopodia or synapses are required to retain the axon, none of the mutants should exhibit axon retractions before P100 (Figure 6C). If we increase the "minimal stabilization" number, i.e., the number of filopodia plus synapses, WT and all mutants exhibit an increasing probability to retract. Wild type and *trio* exhibit the same low probability to retract only if high numbers of filopodia and synapses are required for stabilization (Figure 6C). In contrast, lar, *liprin-α* and *syd-1* all exhibit significantly increased probabilities to retract. Notably, the regimen where only lar, *liprin-α*, and *syd-1* exhibit retractions is robust over a wide range of the "minimal stabilization factor" (Figure 6C). Figures 6H–6K show simulated retraction dynamics of all mutants for the "minimal stabilization" number marked by an arrow in Figure 6C. Remarkably, all mutants exhibited simulated retraction kinetics that closely resembled the observed retractions. In particular, *liprin-α* exhibits slowly decreasing retraction rates, while *syd-1* appears significantly more dampened after P60 (comp. Figures 6B, 6I, and 6J). The least good match is *lar*, where the data show earlier retractions with higher rates than in the model. This suggests that retractions in *lar* are not sufficiently explained by synapse loss but may occur earlier due to an additional adhesion role, as previously suggested (Hakeda-Suzuki et al., 2017; Weng et al., 2011). In sum, our combined live dynamics measurements and data-driven modeling suggest that the serial synapse formation model is sufficient to predict the number and distribution of synapses and their role in stabilizing axon terminals in the wild type, *liprin-α*, *syd-1*, and *trio*. Our data further suggest that Lar plays a role in the same process as Liprin-α and Syd-1, but early retractions may be caused by an additional, earlier function.

DISCUSSION

In this study, we characterized the role of filopodial dynamics during synapse formation using the *Drosophila* R7 photoreceptor terminal as a model. We present a serial synapse formation model based on competitive distribution of synaptic building materials between synaptogenic filopodia (Figure 7).

Serial Synapse Formation through Filopodial Competition for Synaptic Seeding Factors

Our data link bulbous filopodia to synapse formation based on three findings: (1) in the wild type, these are the only filopodia that specifically occur during the time window of synapse formation and do not exhibit stochastic dynamics, and wild-type R7 photoreceptor axons stabilize 1–2 bulbous filopodia at a time; (2) the synaptic seeding factors Liprin-α and Syd-1 non-randomly localize to 1–2 bulbous filopodia at a time; and (3) loss of *liprin-*α or *syd-1* selectively affects the stabilization of bulbous filopodia. Loss of the upstream receptor *lar* similarly selectively affects bulbous filopodia but, in addition to bulb destabilization, also strongly affects bulb initiation. Together, these findings support a model whereby stochastic filopodial exploration leads to bulb stabilization and synapse formation one at a time. In this model, restrictive synaptogenic filopodia formation "paces" the formation of ~25 synapses over 50 h, effectively controlling synapse numbers within the available developmental time window.

The key mechanism of this model is the inhibitory feedback of synaptogenic filopodium formation. In contrast to all other filopodia, the dynamics of bulbous filopodia are not independent events. How are synaptic seeding factors competitively distributed between these filopodia? Our live-imaging data suggest that Liprin-α or Syd-1 can traffic in and out of filopodia but overexpressed proteins accumulate in the axon terminal trunk and do not enter to more than 1–2 filopodia, indicating that trafficking into filopodia is restricted. Morphologically, filopodia are very thin structures that may not provide much space for freely diffusing proteins or organelles. On the other hand, the bulbous tip provides a much larger volume that may be required for sufficient amounts of synaptic seeding factors and other building material to initiate synapse formation. Furthermore, our computational tests show that "winner-takes-all" dynamics can arise from the dynamic distribution of a limited resource that confers a competitive advantage (longer lifetime, which leads to further accumulation) without the need for active filopodial communication (Figures S3 and S4).

Since Syd-1 and Liprin-α are not required for bulb initiation, we speculate that filopodial contact with a synaptic partner may initiate the bulb and precede active zone formation. Our data suggest that Lar is a good candidate for a presynaptic receptor with such a role, but it is unlikely to be the sole upstream receptor. Neurexin (Owald et al., 2012) and PTP69D (Garrity et al., 1999; Hofmeyer and Treisman, 2009), for example, are other known candidates. In the absence of an upstream receptor or the seeding factors themselves, synapse assembly fails and bulbs destabilize. New bulb generation following loss of bulbs in the absence of seeding factors can also be explained with seeding factors as a limiting resource with a competitive advantage (Figures S3 and S4). This is reminiscent of other competitive processes that shape neuronal morphology, e.g., the restricting role of building material in the competitive development of dendritic branches in a motorneuron (Ryglewski et al., 2017). Our mutant analyses suggest that stable bulbs are linked to negative feedback on other bulbs via the function of the RhoGEF Trio. While the exact mechanism is unclear, it is tempting to speculate about a role of actin-dependent signaling downstream of synaptic seeding.

Our current model only considers the presynaptic axon terminal. The main postsynaptic partner of R7 are amacrine-like Dm8 cells, whose elaborate dendritic processes are present in direct vicinity to the R7 filopodia throughout the developmental period of synapse formation (Karuppudurai et al., 2014). We currently do not know the dynamics of the postsynaptic processes and whether they restrict availability or are "easily found" as postsynaptic partners. Our presynaptic model could explain the observed slow, serial synapse formation even in the presence of abundant postsynaptic partner processes.

Cause and Effect: The Challenge to Identify Primary Defects in Circuit Assembly

Mutations in the proposed pathway components Lar, Liprin-α, Syd1, and Trio have been independently characterized for their roles in active zone assembly (mostly at the larval neuromuscular junction) and axon targeting, in large part in the visual system (Astigarraga et al., 2010; Hakeda-Suzuki et al., 2017; Holbrook et al., 2012; Maurel-Zaffran et al., 2001; Weng et al., 2011). It is likely that all four genes exert more than one function in different contexts. Defects in synapse formation and retraction are captured by the measured parameters and our model. However, some differences in overall morphology, including overextensions in the *syd-1* mutant, may be described by parameters not considered in the model, e.g., filopodial length, and due to some differences in their molecular function (Astigarraga et al., 2010; Holbrook et al., 2012). Similarly, for Lar, independent context-dependent functions have been characterized based on different downstream adaptors (Weng et al., 2011).

We asked to what extent a primary role for *lar*, *trio*, *syd-1*, and *liprin-*α in synapse formation could explain previously observed phenotypes. All filopodial defects in the four mutants occur independently and prior to possible retraction events. Our combined live imaging and computational modeling suggests that defects in the *syd-1* and *liprin-*α mutants are consistent with a primary defect in bulb stabilization and synapse formation. These defects may in turn lead to axon destabilization or represent independent functions; *lar* may have an additional earlier adhesion function and *trio* does not play a critical role in the formation of the correct number of synapses, while its effect on general filopodial dynamics may sensitize mutant axons to other changes.

We base our conclusion that Lar, Liprin-α, and Syd-1 have a primary function in synapse formation on three pieces of evidence: (1) all mutants initially target correctly and exhibit normal filopodial dynamics prior to synapse formation; (2) the mutants start retracting only when synaptic contacts initiate, in the order and severity from the receptor to the downstream elements; and (3) all three mutants exhibit the loss of competitive bulb stabilization. Taken together, these observations support a direct role in synapse formation following bulb stabilization, but we cannot exclude other molecular functions. For example, in both *C. elegans* and *Drosophila*, Lar has been shown to function independently in axon guidance and synapse formation (Ackley et al., 2005; Weng et al., 2011). We found that *syd-1*$^{\Delta RhoGAP}$ mutants have normal terminal morphology and only a mild decrease in the number of BrpD3-puncta. This is consistent with recent findings that a RhoGAP-deficient Syd-1 fragment is sufficient to rescue early active zone seeding events at the *Drosophila*

neuromuscular junction but not the recruitment of Brp as the active zones mature (Spinner et al., 2018). However, since homozygous *syd-1*$^{\Delta RhoGAP}$ flies have no obvious connectivity defects, synapse numbers are apparently sufficient for axon terminal stabilization.

Finally, our observations suggest that loss of the primary functions of these proteins in filopodial dynamics and synapse formation are sufficient to cause axon retractions. The phenotypes observed here for lar, *liprin-α*, and *syd-1* are somewhat similar but in contrast to *cadN* only occur at or after the time of synaptic partner identification. While filopodia continuously decrease, synapses continuously increase (Figure 6A), thereby allowing a takeover of the axon terminal stabilization function. The modeling fits the wild type, *liprin-α*, *syd-1*, and *trio* remarkably well. On the other hand, retractions in the *lar* mutant are qualitatively predicted, but the model fails to explain retractions quantitatively. A partial explanation may be that we parameterized our model only based on the *lar* mutant axon terminals that are still unretracted at P60. These are only 30% of terminals by that time, and we have effectively selected for terminals with dynamics that prevented retractions thus far. It is likely that earlier retractions are caused by defects in filopodial adhesion or synaptic contacts. In sum, our data and modeling support a role for synapses in the stabilization of R7 axon terminals, which can lead to probabilistic axon retractions in mutants affecting synapse formation.

STAR★METHODS

Detailed methods are provided in the online version of this paper and include the following:

- KEY RESOURCES TABLE
- LEAD CONTACT AND MATERIALS AVAILABILITY
- EXPERIMENTAL MODEL AND SUBJECT DETAILS
  - Molecular Biology
  - Histology and Fixed Imaging
  - Brain Culture and Live Imaging
  - Electroretinogram (ERG) Recordings
- QUANTIFICATION AND STATISTICAL ANALYSIS
  - Data Analysis
  - Filopodia Tracing and Tracking
  - Mathematical Modeling
  - Identification of State Variables
  - Short-Lived vs. Long-Lived Filopodia
  - Transient vs. Stable (synaptogenic) Bulbous Tip Filopodia
  - Model Selection
  - Final Model
  - Model Parameterization
- DATA AND CODE AVAILABILITY

SUPPLEMENTAL INFORMATION

Supplemental Information can be found online at https://doi.org/10.1016/j.devcel.2019.06.014.

ACKNOWLEDGMENTS

We would like to thank all members of the Hiesinger, Wernet, and Hassan labs for their support and helpful discussions. We thank Stephan Sigrist, Claude Desplan, Iris Salecker, Orkun Akin, and Tory Herman for critical reading of earlier versions of this manuscript. We further thank Thomas Clandinin, Tory Herman, Larry Zipursky, and Stephan Sigrist for reagents. This work was supported by the NIH (RO1EY018884 and RO1EY023333) and the German Research Foundation (DFG, SFB 958 and SFB186) and FU Berlin. M.v.K. acknowledges financial support from the BMBF grant number 031A307, and M.M., M.W., and M.v.K. acknowledge support from MATHEON and the Einstein Center for Mathematics Berlin, provided through the Einstein Stiftung Berlin.

AUTHOR CONTRIBUTIONS

M.N.O., M.v.K., and P.R.H. designed the project. M.N.O, A.K., and A.H. designed and performed all imaging experiments. M.N.O., A.K., A.H., H.W., and F.R.K. performed the experiments. J.B., V.J.D., and S.P. built the filopodia-tracking module. M.M., M.W., and M.v.K. performed the mathematical modeling. M.N.O., A.K., A.H., I.-M.D., M.v.K., and P.R.H. analyzed the data. M.N.O., A.K., A.H., M.v.K, and P.R.H. wrote the paper.

DECLARATION OF INTERESTS

The authors declare no competing interests.

Received: January 14, 2019
Revised: May 15, 2019
Accepted: June 21, 2019
Published: July 25, 2019

REFERENCES

Ackley, B.D., Harrington, R.J., Hudson, M.L., Williams, L., Kenyon, C.J., Chisholm, A.D., and Jin, Y. (2005). The two isoforms of the Caenorhabditis elegans leukocyte-common antigen related receptor tyrosine phosphatase PTP-3 function independently in axon guidance and synapse formation. J. Neurosci. *25*, 7517–7528.

Allen, L.J.S. (2003). An introduction to stochastic processes with applications to biology (Taylor & Francis).

Astigarraga, S., Hofmeyer, K., Farajian, R., and Treisman, J.E. (2010). Three Drosophila liprins interact to control synapse formation. J. Neurosci. *30*, 15358–15368.

Bateman, J., Shu, H., and Van Vactor, D. (2000). The guanine nucleotide exchange factor trio mediates axonal development in the Drosophila embryo. Neuron *26*, 93–106.

Berger-Müller, S., Sugie, A., Takahashi, F., Tavosanis, G., Hakeda-Suzuki, S., and Suzuki, T. (2013). Assessing the role of cell-surface molecules in central synaptogenesis in the Drosophila visual system. PLoS One *8*, e83732.

Brunelli, R. (2009). Computational aspects of template matching. In Template matching techniques in computer vision (John Wiley & Sons, Ltd), pp. 201–219.

Chen, Y., Akin, O., Nern, A., Tsui, C.Y., Pecot, M.Y., and Zipursky, S.L. (2014). Cell-type-specific labeling of synapses in vivo through synaptic tagging with recombination. Neuron *81*, 280–293.

Chien, C.B., Rosenthal, D.E., Harris, W.A., and Holt, C.E. (1993). Navigational errors made by growth cones without filopodia in the embryonic Xenopus brain. Neuron *11*, 237–251.

Choe, K.M., Prakash, S., Bright, A., and Clandinin, T.R. (2006). Liprin-alpha is required for photoreceptor target selection in Drosophila. Proc. Natl. Acad. Sci. USA *103*, 11601–11606.

Clandinin, T.R., Lee, C.H., Herman, T., Lee, R.C., Yang, A.Y., Ovasapyan, S., and Zipursky, S.L. (2001). Drosophila LAR regulates R1-R6 and R7 target specificity in the visual system. Neuron *32*, 237–248.

Cohen-Cory, S. (2002). The developing synapse: construction and modulation of synaptic structures and circuits. Science *298*, 770–776.

Constance, W.D., Mukherjee, A., Fisher, Y.E., Pop, S., Blanc, E., Toyama, Y., and Williams, D.W. (2018). Neurexin and neuroligin-based adhesion

complexes drive axonal arborisation growth independent of synaptic activity. Elife *7*.

Dai, Y., Taru, H., Deken, S.L., Grill, B., Ackley, B., Nonet, M.L., and Jin, Y. (2006). SYD-2 liprin-alpha organizes presynaptic active zone formation through ELKS. Nat. Neurosci. *9*, 1479–1487.

Debant, A., Serra-Pagès, C., Seipel, K., O'Brien, S., Tang, M., Park, S.H., and Streuli, M. (1996). The multidomain protein Trio binds the LAR transmembrane tyrosine phosphatase, contains a protein kinase domain, and has separate rac-specific and rho-specific guanine nucleotide exchange factor domains. Proc. Natl. Acad. Sci. USA *93*, 5466–5471.

Dercksen, V.J., Hege, H.C., and Oberlaender, M. (2014). The Filament Editor: an interactive software environment for visualization, proof-editing and analysis of 3D neuron morphology. Neuroinformatics *12*, 325–339.

Dunah, A.W., Hueske, E., Wyszynski, M., Hoogenraad, C.C., Jaworski, J., Pak, D.T., Simonetta, A., Liu, G., and Sheng, M. (2005). LAR receptor protein tyrosine phosphatases in the development and maintenance of excitatory synapses. Nat. Neurosci. *8*, 458–467.

Fouquet, W., Owald, D., Wichmann, C., Mertel, S., Depner, H., Dyba, M., Hallermann, S., Kittel, R.J., Eimer, S., and Sigrist, S.J. (2009). Maturation of active zone assembly by Drosophila Bruchpilot. J. Cell Biol. *186*, 129–145.

Gadgil, C., Lee, C.H., and Othmer, H.G. (2005). A stochastic analysis of first-order reaction networks. Bull. Math. Biol. *67*, 901–946.

Garrity, P.A., Lee, C.H., Salecker, I., Robertson, H.C., Desai, C.J., Zinn, K., and Zipursky, S.L. (1999). Retinal axon target selection in Drosophila is regulated by a receptor protein tyrosine phosphatase. Neuron *22*, 707–717.

Hakeda-Suzuki, S., Takechi, H., Kawamura, H., and Suzuki, T. (2017). Two receptor tyrosine phosphatases dictate the depth of axonal stabilizing layer in the visual system. Elife *6*.

Hallam, S.J., Goncharov, A., McEwen, J., Baran, R., and Jin, Y. (2002). SYD-1, a presynaptic protein with PDZ, C2 and rhoGAP-like domains, specifies axon identity in C. elegans. Nat. Neurosci. *5*, 1137–1146.

Hiesinger, P.R., Zhai, R.G., Zhou, Y., Koh, T.W., Mehta, S.Q., Schulze, K.L., Cao, Y., Verstreken, P., Clandinin, T.R., Fischbach, K.F., et al. (2006). Activity-independent prespecification of synaptic partners in the visual map of Drosophila. Curr. Biol. *16*, 1835–1843.

Hofmeyer, K., Maurel-Zaffran, C., Sink, H., and Treisman, J.E. (2006). Liprin-alpha has LAR-independent functions in R7 photoreceptor axon targeting. Proc. Natl. Acad. Sci. USA *103*, 11595–11600.

Hofmeyer, K., and Treisman, J.E. (2009). The receptor protein tyrosine phosphatase LAR promotes R7 photoreceptor axon targeting by a phosphatase-independent signaling mechanism. Proc. Natl. Acad. Sci. USA *106*, 19399–19404.

Holbrook, S., Finley, J.K., Lyons, E.L., and Herman, T.G. (2012). Loss of syd-1 from R7 neurons disrupts two distinct phases of presynaptic development. J. Neurosci. *32*, 18101–18111.

Karuppudurai, T., Lin, T.Y., Ting, C.Y., Pursley, R., Melnattur, K.V., Diao, F., White, B.H., Macpherson, L.J., Gallio, M., Pohida, T., et al. (2014). A hard-wired glutamatergic circuit pools and relays UV signals to mediate spectral preference in Drosophila. Neuron *81*, 603–615.

Kaufmann, N., DeProto, J., Ranjan, R., Wan, H., and Van Vactor, D. (2002). Drosophila liprin-alpha and the receptor phosphatase Dlar control synapse morphogenesis. Neuron *34*, 27–38.

Lee, C.H., Herman, T., Clandinin, T.R., Lee, R., and Zipursky, S.L. (2001). N-cadherin regulates target specificity in the Drosophila visual system. Neuron *30*, 437–450.

Lee, T., and Luo, L. (1999). Mosaic analysis with a repressible cell marker for studies of gene function in neuronal morphogenesis. Neuron *22*, 451–461.

Mason, C., and Erskine, L. (2000). Growth cone form, behavior, and interactions in vivo: retinal axon pathfinding as a model. J. Neurobiol. *44*, 260–270.

Maurel-Zaffran, C., Suzuki, T., Gahmon, G., Treisman, J.E., and Dickson, B.J. (2001). Cell-autonomous and -Nonautonomous functions of LAR in R7 photoreceptor axon targeting. Neuron *32*, 225–235.

Meyer, M.P., and Smith, S.J. (2006). Evidence from in vivo imaging that synaptogenesis guides the growth and branching of axonal arbors by two distinct mechanisms. J. Neurosci. *26*, 3604–3614.

Newsome, T.P., Asling, B., and Dickson, B.J. (2000a). Analysis of *Drosophila* photoreceptor axon guidance in eye-specific mosaics. Development. *127*, 851–860.

Newsome, T.P., Schmidt, S., Dietzl, G., Keleman, K., Asling, B., Debant, A., and Dickson, B.J. (2000b). Trio combines with dock to regulate Pak activity during photoreceptor axon pathfinding in Drosophila. Cell *101*, 283–294.

Owald, D., Fouquet, W., Schmidt, M., Wichmann, C., Mertel, S., Depner, H., Christiansen, F., Zube, C., Quentin, C., Körner, J., et al. (2010). A Syd-1 homologue regulates pre- and postsynaptic maturation in Drosophila. J. Cell Biol. *188*, 565–579.

Owald, D., Khorramshahi, O., Gupta, V.K., Banovic, D., Depner, H., Fouquet, W., Wichmann, C., Mertel, S., Eimer, S., Reynolds, E., et al. (2012). Cooperation of Syd-1 with neurexin synchronizes pre- with postsynaptic assembly. Nat. Neurosci. *15*, 1219–1226.

Owald, D., and Sigrist, S.J. (2009). Assembling the presynaptic active zone. Curr. Opin. Neurobiol. *19*, 311–318.

Özel, M.N., Langen, M., Hassan, B.A., and Hiesinger, P.R. (2015). Filopodial dynamics and growth cone stabilization in Drosophila visual circuit development. Elife *4*.

Ryglewski, S., Vonhoff, F., Scheckel, K., and Duch, C. (2017). Intra-neuronal competition for Synaptic Partners conserves the amount of dendritic building material. Neuron *93*, 632–645.e6.

Sanes, J.R., and Yamagata, M. (2009). Many paths to synaptic specificity. Annu. Rev. Cell Dev. Biol. *25*, 161–195.

Sato, M., Bitter, I., Bender, M.A., Kaufman, A.E., and Nakajima, M. (2000). TEASAR: tree-structure extraction algorithm for accurate and robust skeletons. Paper presented at: Proceedings therapeutic eighth Pacific conference on computer graphics and applications.

Schmid, A., Hallermann, S., Kittel, R.J., Khorramshahi, O., Frölich, A.M., Quentin, C., Rasse, T.M., Mertel, S., Heckmann, M., and Sigrist, S.J. (2008). Activity-dependent site-specific changes of glutamate receptor composition in vivo. Nat. Neurosci. *11*, 659–666.

Schoch, S., and Gundelfinger, E.D. (2006). Molecular organization of the presynaptic active zone. Cell Tissue Res. *326*, 379–391.

Serra-Pagès, C., Kedersha, N.L., Fazikas, L., Medley, Q., Debant, A., and Streuli, M. (1995). The LAR transmembrane protein tyrosine phosphatase and a coiled-coil LAR-interacting protein co-localize at focal adhesions. EMBO J. *14*, 2827–2838.

Spinner, M.A., Walla, D.A., and Herman, T.G. (2018). Drosophila Syd-1 has RhoGAP activity that is required for presynaptic clustering of Bruchpilot/ELKS but not Neurexin-1. Genetics *208*, 705–716.

Sugie, A., Hakeda-Suzuki, S., Suzuki, E., Silies, M., Shimozono, M., Möhl, C., Suzuki, T., and Tavosanis, G. (2015). Molecular remodeling of the presynaptic active zone of Drosophila photoreceptors via activity-dependent feedback. Neuron *86*, 711–725.

Takemura, S.Y., Bharioke, A., Lu, Z., Nern, A., Vitaladevuni, S., Rivlin, P.K., Katz, W.T., Olbris, D.J., Plaza, S.M., Winston, P., et al. (2013). A visual motion detection circuit suggested by Drosophila connectomics. Nature *500*, 175–181.

Vaughn, J.E., Henrikson, C.K., and Grieshaber, J.A. (1974). A quantitative study of synapses on motor neuron dendritic growth cones in developing mouse spinal cord. J. Cell Biol. *60*, 664–672.

Wagh, D.A., Rasse, T.M., Asan, E., Hofbauer, A., Schwenkert, I., Dürrbeck, H., Buchner, S., Dabauvalle, M.C., Schmidt, M., Qin, G., et al. (2006). Bruchpilot, a protein with homology to ELKS/CAST, is required for structural integrity and function of synaptic active zones in Drosophila. Neuron *49*, 833–844.

Wang, Y., Liu, X., Biederer, T., and Südhof, T.C. (2002). A family of RIM-binding proteins regulated by alternative splicing: implications for the genesis of synaptic active zones. Proc. Natl. Acad. Sci. USA *99*, 14464–14469.

Weng, Y.L., Liu, N., DiAntonio, A., and Broihier, H.T. (2011). The cytoplasmic adaptor protein Caskin mediates lar signal transduction during Drosophila motor axon guidance. J. Neurosci. *31*, 4421–4433.

Wentzel, C., Sommer, J.E., Nair, R., Stiefvater, A., Sibarita, J.B., and Scheiffele, P. (2013). mSYD1A, a mammalian synapse-defective-1 protein, regulates synaptogenic signaling and vesicle docking. Neuron *78*, 1012–1023.

Williamson, W.R., Wang, D., Haberman, A.S., and Hiesinger, P.R. (2010). A dual function of V0-ATPase a1 provides an endolysosomal degradation mechanism in Drosophila melanogaster photoreceptors. J. Cell Biol. *189*, 885–899.

Wills, Z., Bateman, J., Korey, C.A., Comer, A., and Van Vactor, D. (1999). The tyrosine kinase Abl and its substrate enabled collaborate with the receptor phosphatase Dlar to control motor axon guidance. Neuron *22*, 301–312.

Xu, Y., Taru, H., Jin, Y., and Quinn, C.C. (2015). SYD-1C, UNC-40 (DCC) and SAX-3 (Robo) function interdependently to promote axon guidance by regulating the MIG-2 GTPase. PLoS Genet. *11*, e1005185.

Yogev, S., and Shen, K. (2014). Cellular and molecular mechanisms of synaptic specificity. Annu. Rev. Cell Dev. Biol. *30*, 417–437.

Zhen, M., and Jin, Y. (1999). The liprin protein SYD-2 regulates the differentiation of presynaptic termini in C. elegans. Nature *401*, 371–375.

Ziv, N.E., and Smith, S.J. (1996). Evidence for a role of dendritic filopodia in synaptogenesis and spine formation. Neuron *17*, 91–102.

STAR★METHODS

KEY RESOURCES TABLE

REAGENT or RESOURCE	SOURCE	IDENTIFIER
Chemicals, Peptides, and Recombinant Proteins		
Vectashield	Vector Laboratories	H-1000
PBS	Gibco	70011-36
Formaldehyde	Merck KgaA	1.03999.1000
Triton X-100	Sigma-Aldrich	T8787
Schneider's *Drosophila* Medium [+] L-Glutamine	Gibco	21720-024
Agarose, low gelling temperature	Sigma-Aldrich	A9045-10G
Human insulin recombinant zinc	Gibco	12585014
Penicillin/Streptomycin	Gibco	15140122
ES Cell FBS	Gibco	16141-061
20-Hydroxyecdysone	Sigma-Aldrich	5289-74-7
SilGard and Silicone Elastomer Kit	Dow Corning	184
Experimental Model: Organisms/Strains		
Drosophila, GMR-FLP (X)	Lee et al., 2001	N/A
Drosophila, hs-FLP (X)	Bloomington *Drosophila* Stock Center (BDSC)	8862
Drosophila, GMR-Gal4 (II)	(BDSC)	1104
Drosophila, GMR-Gal4 (III)	BDSC	29967
Drosophila, GMR-FRT-stop-FRT-Gal4 (II)	Chen et al., 2014	N/A
Drosophila, FRT80B, tub-Gal80	BDSC	5191
Drosophila, FRT82B, tub-Gal80	BDSC	5135
Drosophila, FRT42D, GMR-Gal80	This paper. GMR-Gal80: Gift from Thomas Clandinin.	N/A
Drosophila, FRT40A, tub-Gal80	BDSC	5192
Drosophila, FRT2A, tub-Gal80	BDSC	5190
Drosophila, FRT40A	BDSC	8212
Drosophila, FRT42D	BDSC	1802
Drosophila, FRT80B	BDSC	8214
Drosophila, FRT82B	BDSC	5619
Drosophila, FRT2A	BDSC	1997
Drosophila, FRT82B, *syd-1*^{w46}	Holbrook et al., 2012	N/A
Drosophila, FRT82B, *syd-1*^{dRhoGAP}	This paper.	N/A
Drosophila, FRT40A, *liprin-*α^{E}	Choe et al., 2006	N/A
Drosophila, FRT40A, *lar*^{2127}	Maurel-Zaffran et al., 2001	N/A
Drosophila, UAS-lar RNAi	Vienna *Drosophila* Research Center (VDRC)	36269
Drosophila, FRT2A, *trio*^{3}	Newsome et al., 2000a	9130
Drosophila, / UAS-Brp-RNAi^{B3}, UAS-Brp-RNAi^{C8}	Wagh et al., 2006	N/A
Drosophila, UAS-CD4-tdGFP (II)	BDSC	35839
Drosophila, UAS-CD4-tdGFP (III)	BDSC	35836
Drosophila, UAS-CD4-tdTomato (III)	BDSC	35837
Drosophila, UAS-BrpD3-GFP	Schmid et al., 2008	N/A
Drosophila, UAS-BrpD3-mKate2 (II and III)	This paper.	N/A
Drosophila, UAS-Liprinα-GFP	Fouquet et al., 2009	N/A
Drosophila, UAS-myc-Liprin	BDSC	63809
Drosophila, UAS-GFP-Syd1 (II).	Owald et al., 2010	N/A
Drosophila, UAS-GFP-Syd1 (III).	Stephan Sigrist (unpublished)	N/A
Drosophila, GMR-myr-tdTomato (II and III)	Gift from S.Lawrence Zipursky	N/A

(*Continued on next page*)

Continued

REAGENT or RESOURCE	SOURCE	IDENTIFIER
Antibodies		
Mouse anti-Chaoptin	Developmental Studies Hybridoma Bank (DSHB)	24B10
Mouse anti-lar	DSHB	9D82B3
Mouse anti-Trio	DSHB	9.4A anti-Trio
Myc-Tag (71D10) Rabbit mAb	Cell Signaling Technology	2278T
Cy™3 AffiniPure Goat Anti-Mouse IgG (H+L)	Jackson Laboratories	115-165-166
Cy™5 AffiniPure Goat Anti-Mouse IgG (H+L)	Jackson Laboratories	115-175-166
Goat anti-Mouse IgG (H+L) Alexa Fluor 647	Thermofisher Scientific	A28181
Recombinant DNA		
pTW BrpD3-GFP	Schmid et al., 2008	N/A
pmKate2-C	Evrogen	FP181
Software and Algorithms		
ImageJ	National Institutes of Health (NIH)	N/A
Imaris	Bitplane, Switzerland	N/A
GraphPad Prism	GraphPad Software, La Jolla, USA	N/A
Microvolution Plug-in	Microvolution	N/A
Clampfit	Axon Instruments	N/A
Clampex	Axon Instruments	N/A
MATLAB	Mathworks	N/A
Amira ZIB Edition	Zuse Institut Berlin	N/A

LEAD CONTACT AND MATERIALS AVAILABILITY

Reagents generated in this study are available for distribution. Requests for resources and reagents should be directed to Robin Hiesinger (robin.hiesinger@fu-berlin.de).

EXPERIMENTAL MODEL AND SUBJECT DETAILS

All experiments were performed with *Drosophila* pupae collected at P+0% (white pupae) and aged in 25°C unless otherwise specified. We did not select for gender in any of the imaging experiments. Source details for all fly lines are specified in the Key Resources Table.

Following final genotypes were used for each experiment: For wild-type membrane and synapse imaging: (GMR-FLP/+; GMR-Gal4/ GMR-myr-tdTomato; FRT80B, UAS-CD4-tdGFP/ FRT80B, tub-Gal80) and (GMR-FLP/+; FRT42D, GMR-Gal80/ FRT42D; GMR-Gal4, UAS-CD4-tdTomato/ UAS-BrpD3-GFP). Membrane imaging with mutants: (GMR-FLP/+; FRT40A, tub-Gal80/ FRT40A, *liprin-*α^{E} (or *dlar*^{2127}); GMR-Gal4, UAS-CD4-tdGFP, GMR-myr-tdTomato/+), (GMR-FLP/+; GMR-Gal4, UAS-CD4-tdGFP/ GMR-myr-tdTomato; FRT82B, tub-Gal80/ FRT82B, *syd-1*^{w46} (or *syd-1*^{dRhoGAP})), (GMR-FLP/+; GMR-Gal4, UAS-CD4-tdGFP/ GMR-myr-tdTomato; FRT2A, tub-Gal80/ FRT2A, *trio*^{3}). Synaptic imaging with mutants and corresponding controls: (GMR-FLP/+; FRT40A, tub-Gal80/ FRT40A, *liprin-*α^{E} (or *dlar*^{2127} or FRT40A only); GMR-Gal4, UAS-CD4-tdTomato/ UAS-BrpD3-GFP), (GMR-FLP/+; GMR-Gal4, UAS-CD4-tdGFP/ UAS-BrpD3-mKate2; FRT82B, tub-Gal80/ FRT82B, *syd-1*^{w46} (or *syd-1*^{dRhoGAP} or FRT82B only)), (GMR-FLP/+; GMR-Gal4, UAS-CD4-tdGFP/ UAS-BrpD3-mKate2; FRT2A, tub-Gal80/ FRT2A, *trio*^{3} (or FRT2A only)). For imaging of early synaptic markers: (hs-FLP/+; GMR-FRT-w^{+}-FRT-Gal4/ UAS-Liprin-α-GFP (or UAS-GFP-Syd1), UAS-CD4-tdTomato). For visualizing early synaptic markers in *trio* mutant axons GMR-FLP; LGMR Gal4, UAS-CD4tdTom/ UAS-liprin-α-GFP (or UAS-GFP-Syd-1); FRT2A (or FRT2A *trio3*)/ FRT2A, tub-Gal80. For visualizing early synaptic markers in *lar* mutant axons (GMR-FLP/+; FRT40A, *dlar*^{2127}/ FRT40A, Tub-Gal80; GMR-Gal4, UAS-CD4tdTomato/+, and ;UAS-lar RNAi, UAS-Liprin-α-GFP/+; GMR-Gal4/+). For imaging with Brp RNAi: (GMR-FLP/+; FRT42D, GMR-Gal80/ FRT42D; GMR-Gal4, UAS-CD4-tdGFP, GMR-myr-tdTomato/ UAS-Brp-RNAi^{B3}, UAS-Brp-RNAi^{C8}). For ERG recordings: (; GMR-Gal4/ FRT42D ;) and (; GMR-Gal4/ FRT42D; UAS-Brp-RNAi^{B3}, UAS-Brp-RNAi^{C8}/ +).

Molecular Biology

To build the UAS-BrpD3-mKate2 construct, EGFP sequence was removed from the pTW BrpD3-GFP plasmid (gift from S. Sigrist) using Xba1 and Age1 sites. mKate2 sequence was amplified from the pmKate2-C plasmid (Evrogen) using the following forward

and reverse primers (respectively): gggTCTAGACggtggaggaggtATGGTGAGCGAGCTGATTAA and cccACCGGTTTATCTGTGCC CCAGTTTGCTAG. The products were digested with Xba1 and Age1 and ligated into the above-mentioned pTW BrpD3 plasmid. Injections were done by Rainbow Transgenics (USA) for P-element insertion and candidate lines were isolated and tested according to standard procedures.

syd-1^{dRhoGAP} allele was generated by Well Genetics (Taiwan) using CRISPR/Cas9 Scarless (DsRed) system (Figure S5D). 2 gRNAs were used against the following target sites (PAM): CGGGAGTCTAAGAATGCTCC[CGG]; AGATACTTAAGCACCGCGAT[CGG]. Upon PBac-mediated excision, a specific and complete deletion of the RhoGAP domain was achieved with only a TTAA motif left embedded in the exogenous sequence GTTAAA (Figure S5E). Insertion and excisions were verified by genomic PCR and sequencing. Full design details and sequencing results are available upon request.

Histology and Fixed Imaging

Eye-brain complexes were dissected in PBS, fixed in 3.7% paraformaldehyde (PFA) in PBS for 40 min, washed in PBST (0.4% Triton-X) and mounted in Vectashield (Vector Laboratories, CA). Images were collected using a Leica TCS SP8-X white laser confocal microscope with a 63X glycerol objective (NA=1.3).

Following antibodies were used for fixed imaging: Primary antibodies: anti-Trio (mouse, 1:50, DSHB), 24B10 (1:200, DSHB), anti-myc (1:200, Cell signaling), anti-Lar (mouse, 1:50, DSHB), anti-Syd-1 (rabbit, 1:500, gift from Stephan Sigrist).

Secondary antibodies: anti-mouse Alexa 647 (1:500, Life technologies), anti-mouse Cy5 (1:500, Jackson laboratories), anti-mouse-Cy3 (1:500, Jackson Laboratories), anti-Rabbit Alexa 647 (1:500, Life Technologies), anti-Rabbit Cy5 (1:500, Jackson Laboratories).

Brain Culture and Live Imaging

Ex vivo eye-brain complexes were prepared as described before (Özel et al., 2015). For filopodial imaging, brains were dissected at P+40% and 1 μg/ml 20-Hydroxyecdysone was included in the culture media. For synaptic imaging, brains were dissected at P+50% and no ecdysone was included.

Live imaging was performed using a Leica SP8 MP microscope with a 40X IRAPO water objective (NA=1.1) with a Chameleon Ti:Sapphire laser and Optical Parametric Oscillator (Coherent). We used a single excitation laser at 950 nm for two-color GFP/Tomato imaging. For GFP/mKate2 imaging lasers were set to 890 nm (pump) and 1150 nm (OPO).

GFP-Syd-1 and Liprin-alpha-GFP overexpression did not obviously affect filopodial dynamics (Video S3).

Electroretinogram (ERG) Recordings

1-5 day-old adult flies were reversibly glued on slides using nontoxic school glue. Flies were exposed to 1s pulses of light stimulus provided by computer-controlled white light-emitting diode system (MC1500; Schott) as previously reported (Williamson et al., 2010). ERGs were recorded using Clampex (Axon Instruments) and measured using Clampfit (Axon Instruments).

QUANTIFICATION AND STATISTICAL ANALYSIS

Data Analysis

All live imaging data as well as all data involving synaptic markers were deconvolved (10 iterations with the theoretical PSF) using Microvolution Fiji Extension. Imaging data were analyzed and presented with Imaris (Bitplane). For synaptic counts, Spot objects were created from the BrpD3 channel and Surfaces were generated from the CD4 channel using identical parameters between experimental conditions and the corresponding control. Spots were then filtered for their localization on the positive clones by the Imaris 9 MATLAB extension 'XTSpotsCloseToSurface'.

Further analysis regarding the quantified data and generation of corresponding graphs were done using Prism 7 (GraphPad). Where needed statistical differences were calculated with unpaired, parametric t-tests.

Filopodia Tracing and Tracking

We developed an extension to the Amira Filament Editor (Dercksen et al., 2014) for tracing and tracking of individual filopodia in 4D datasets. Growth cones are represented by an annotated skeleton tree, in which each branch corresponds to a filopodium (Figure S1B). This tree is traced for each time step and matched to the tree in the previous time step in a semi-automatic process.

First, the user interactively marks the growth cone (GC) centers in the first time step. The GC centers are automatically detected in the remaining time steps using template matching (Brunelli, 2009). Then, the GCs are processed one at a time. To this end, the images are cropped such that they contain only the current GC. The user interactively specifies the filopodia tips in the first time step. The filopodia are traced automatically from the tip to the GC center using an intensity-weighted Dijkstra shortest path algorithm based on (Sato et al., 2000). The onset of a filopodium is determined by identifying the point on the path where the 2D intensity profile orthogonal to the tracing changes from Gaussian (for the filopodium) to non-Gaussian (inside the GC body). The user visually verifies the tracing and, if necessary, interactively corrects it using dedicated tools provided by the Filament Editor. After tracing all filopodia in the first time step, they are automatically propagated to the next time step by template matching of tips and onsets, and tracing paths from tip to center through the onset. Propagated filopodia obtain the same track ID as the original. After each time step the user

verifies the generated tracings, and adds newly emerging filopodia. This process is continued until all time steps have been processed (Figure S1A).

Statistical quantities including length, angle, extension/retraction events, and lifetime are extracted from the filopodia geometry and stored in spreadsheets.

Mathematical Modeling

Stochastic filopodial dynamics were modeled by a Poisson process formalism motivated by the observed stochastic dynamics of filopodia (Figure 1F). A model based on suppression of filopodia by synapses did not explain the non-Poisson distribution of bulbous filopodia seen in Figure 1H (see Mathematical Modeling in STAR Methods for details). In addition, mutants that block synapse formation should maintain high levels of filopodia throughout development due to loss of feedback, which is not consistent with the mutant data shown below. Hence, a model in which synapses suppress filopodia could not be reconciled with the measured data. We therefore developed a data-driven minimal model capturing the dynamics of filopodia, bulbous tips and synapse formation. We first identified the systems variables, followed by parallel model selection and parameter estimation, testing higher complexity models whenever the best fit of a simpler model could not sufficiently explain the data. All data used for model inference and parameterization, as well as the parameter inference procedure are outlined below. All codes were written in MATLAB 2018a (Mathworks, Nattick). Parameter inference was performed using the MATLAB 2018a function "fminsearch" and simulations were performed using the stochastic simulation algorithm.

Identification of State Variables

Besides synapses (S), which denote the endpoint of the modelling pipeline, bulbous tips were directly identified in the time-lapse data based on their altered morphology. Analysis of the bulbous lifetime data in wild type and mutants identified two populations: short-lived, unstable bulbous tips (sB) that appeared and disappeared within the 60 min imaging interval vs. stable bulbous tips that persisted for more than 40 min, termed "synaptogenic bulbous tips" (synB) (Figures S9A–S9E). Finally, we identified two types of filopodia, which are distinguished by their lifetime and which will henceforth be denoted short-lived- (sF) and long-lived (F) filopodia, as described below (Figures S9F and S9G).

Short-Lived vs. Long-Lived Filopodia

Our 4D filopodia tracking of 27,390 individual filopodia at P40 and P60 provided the trajectory data for statistical analyses of filopodia lifetimes (Figure S1). We first tested whether the measured dynamics could be represented as a single population or two distinct subpopulations. Figures S9F and S9G shows the respective fits with exponential lifetime distributions, which strongly support the existence of two populations based on the lifetime data (AIC_{2cmp} = 260 (three parameters) versus AIC_{1cmp} = 827 (one parameter)). The respective rate constants for retraction are $c_{2,sF}$= 0.69 (min^{-1}) and $c_{2,\ell F}$= 0.12 (min^{-1}) for short- and long-lived filopodia. The optimal cut-off to differentiate these two populations based on their lifetimes is 8 min (Figure S9G, inset).

Transient vs. Stable (synaptogenic) Bulbous Tip Filopodia

Analysis of the bulbous filopodia lifetime data in the mutants identified two populations: short-lived bulbous tips (sB) and stable bulbous tips that persisted once they appeared (synB) (Figures S9A–S9E). In the wild type, almost all bulbous tips were of the synB type. For the mutants, the lifetime distribution of the short-lived bulbous tips (left bars in Figures S9B–S9E) appeared exponentially distributed with mean lifetimes as follows: *lar* = 3.3 min, *liprin*-alpha = 9 min, *syd-1* = 5.9 min and *trio* = 7.6 min.

Model Selection

We first built a reference model for wild type and then adapted the model parameters to the mutants *syd-1*, *liprin-alpha*, *lar* and *trio* in a data-driven fashion. We tested several structural models and eliminated those that were inconsistent with measured data. For example, we initially tested a model in which synapse formation downregulates the number of filopodia. While this model could explain the wild type data, it failed to explain the downregulation of filopodia in mutants with compromised synapse formation capabilities (*syd-1*, *liprin-alpha*, *lar*). Consequently, this model, and all models in which synapse formation downregulates filopodia, were excluded.

Final Model

The final model is depicted in Figure 3A and its reaction stoichiometries are determined by the following reaction schemes:

$$R_{1,sF}: \varnothing \rightarrow sF, \quad R_{2,sF}: sF \rightarrow \varnothing, \quad R_{1,\ell F}: \varnothing \rightarrow \ell F, \quad R_{2,\ell F}: \ell F \rightarrow \varnothing$$

$$R_3: F \rightarrow sB, \quad R_4: sB \rightarrow \varnothing, \quad R_5: sB \rightarrow synB, \quad R_6: synB \rightarrow S$$

Note that in R_3 we denote by F any filopodium (short-lived and long-lived) and in R_4 we have ignored the flux back into the filopodia compartment $sF + \ell F$ as it insignificantly affects the number number of filopodia (small B, small rate r_4). In the following, we will guide through the model building and parameterization process.

Model Parameterization

Retraction and Generation of Filopodia, r_1, r_2

The exponential lifetimes of both short-lived and long-lived filopodia populations indicate a first-order decay with the respective rate constants $c_{2,sF} = 0.69$ (min^{-1}) and $c_{2,\ell F} = 0.12$ (min^{-1}). In addition, the number of filopodia per time instance is Poisson distributed (Figure 1F), i.e. $sF \sim \mathcal{P}(\lambda_{sF})$ and $\ell F \sim \mathcal{P}(\lambda_{\ell F})$, where λ denotes the average number of filopodia per time instance. Given the first-order retraction of filopodia, the Poisson distribution can be explained by a zero-order input with rate $c_{1,sF}$ and $c_{1,\ell F}$ and $\lambda_{sF} = c_{1,sF}/c_{2,sF}$ and $\lambda_{\ell F} = c_{1,\ell F}/c_{2,\ell F}$ respectively. The latter is a well-established result for the stationary distribution of a birth-death process (Allen, 2003). The average number of filopodia decreased significantly over the 20 h window from P40 to P60 (Figure 1F, see Table below).

	short-lived		long-lived	
Mutant	P40	P60	P40	P60
wt	5.6(3.9)	3.4(1.8)	10(3.5)	4.9(2)
dlar	3.8(2.3)	2.2(1.7)	13(2.3)	5.2(1.6)
lirin-α	4.5(2.7)	2.6(1.5)	8.6(2.1)	6.5(1.9)
syd-1	4.1(2)	1.6(1.3)	9.3(3.3)	3.8(1.7)
trio	6.8(2.8)	4.5(2.2)	14(3.7)	10(2.7)

Average (standard deviation) numbers of short-lived and long-lived filopodia per time instance.

This prompted us to introduce a time-dependent function $f_F(t)$ that down-regulates the generation of new filopodia at a slow time scale. The time-dependent function $f_F(t)$ was then fitted to normalized filopodia counts at P40–P100, as shown in Figure 3B. In summary, the propensity functions for reactions $R_{1,sF}$, $R_{2,sF}$,$R_{1,tF}$, $R_{2,tF}$ are given as follows.

$$r_{1,sF}(t) = f_F(t) \cdot c_{1,sF}, \quad r_{2,sF}(sF) = sF \cdot c_{2,sF}$$

$$r_{1,\ell F}(t) = f_F(t) \cdot c_{1,\ell F}, \quad r_{2,s\ell}(sF) = \ell F \cdot c_{2,\ell F}$$

where $f_F(t) = \max(0, \sum_{i=0}^{5} p_i \cdot t^i)$ is a fifth-order polynome with coefficients $p_5 = -2.97 \cdot 10^{-14}$, $p_4 = 3.31 \cdot 10^{-13}$, $p_3 = -1.29 \cdot 10^{-9}$, $p_2 = 2.06 \cdot 10^{-6}$, $p_1 = -1.45 \cdot 10^{-3}$ and $p_0 = 1$. Note, that t denotes the time in (min) after P40 (e.g. $t_{P40} = 0$). Consequently, we have $f_F(t_{P40}) = 1$ and we can determine the input rate constant directly from the average number of filopodia at P40, i.e. $c_{1,sF} = \lambda_{sF,P40} \cdot c_{2,sF}$ and $c_{1,\ell F} = \lambda_{\ell F,P40} \cdot c_{2,\ell F}$ respectively.

$$* \underset{r_4}{\overset{r_3}{\rightleftharpoons}} sB \xrightarrow{r_5} synB \xrightarrow{r_6} *$$

Bulbous dynamics, r3, r4 and r5

Under the assumption that short-lived unstable bulbous tips retracted by first order kinetics (reaction r_4), the rate constant of retraction is equal to the inverse of the expected lifetimes of bulbous tips. We then wanted to investigate whether the bulbous tip number distributions in Figures 1H, 4D, and 5D can be explained by simple input-output relations or whether regulatory/feedback mechanisms are involved. The number distribution of short-lived bulbous tips sB and synaptogenic (stabilized) bulbous tips synB is given by:

Model I: No Feedback

In the absence of any regulatory mechanisms (feedbacks), all reaction rates are of first order, e.g. $r_4 = sB \cdot c_4$, $r_5 = sB \cdot c_5$ and $r_6 = synB \cdot c_6$. The net influx r_3 at t = P60 is $r_3(t) = c_3(sF(t) + \ell F(t)) \cdot f_{FB}(t)$, where we assume that $sF(t), \ell F(t)$ and $f_{FB}(t)$ are approximately constant over the time scale of interest. Parameters c_4 can be approximated by (the inverse of) the bulbous tip life times and $c_6 = 1/120$ (min^{-1}) can be approximated from the maximum slope of synapse generation presented in Figures 3F and 3G. The two parameters c_5 and $r_3(t)$ remain to be estimated for t = P60.

To perform this task we set up a generator matrix G that has entries (transition rates):

$$G([i,j],[i-1,j]) = i \cdot c_4, \quad G([i,j],[i,j-1]) = j \cdot c_6$$

$$G([i,j],[i+1,j]) = r_3(t), \quad G([i,j],[i,j+1]) = j \cdot c_5$$

and diagonal elements such that the row sum equals 0. In the notation above, the tupel [i, j] denotes the state where *i* short- lived bulbous tips *sB* and *j* synaptogenic bulbous tips *synB* are present. The generator above has a reflecting boundary at sufficiently large N (maximum number of bulbous tips). The stationary distribution of this model is derived by solving the eigenvalue problem

$$G^T \cdot v = v \cdot \lambda$$

and finding the eigenvector corresponding to eigenvalue $\lambda_0 = 0$. From this stationary distribution, we compute the marginal densities of *sB* and *synB* (e.g. summing over all states where i = 0, 1, ... for sB) and fit them to the experimentally derived frequencies (Figures 1H, 4D, and 5D) by minimizing the Kullback-Leibler divergence between the experimental and model-pre-

dicted distributions. The resulting best fit for the wild type is shown in Figure 1H (dashed lines). Lastly, parameter c_3 is derived by calculating

$$c_3 = \frac{r_3(t)}{(sF(t) + \ell F(t)) \cdot f_{FB}(t, t_{1/2})} \quad \text{(Equation 1)}$$

where $sF(t) = f_F(t) \cdot sF(t_{P40})$ and where we assumed that $f_{FB}(t)$ is a tanh function with

$$f_{FB}(t, t_{1/2}) = \frac{1}{2}\left(1 + tanh\left[\frac{3}{t_{1/2}}\ (t - t_{1/2})\right]\right)$$

that models a time-dependent increase in the propensity to form bulbous tips. We had set $t_{1/2}$ = 1000 (min), such that the rate of bulbous formation peaks at P60–P80. Note that for this particular (linear) model, one can also fit r3(t) and c5 to the marginal distributions of sB, synB, such that $sB \sim \mathcal{P}(\lambda_1)$ and $synB \sim \mathcal{P}(\lambda_2)$ with $\lambda_1 = r_3/(c_4 + c_5)$ and $\lambda_2 = \lambda_1 \cdot c_5/c_4$.

Model II: Feedback on bulb generation

We followed the analogous procedure as for model I, except that we incorporated a feedback mechanisms into the generator matrix

$$G([i,j],[i-1,j]) = i \cdot c_4, \qquad G([i,j],[i,j-1]) = j \cdot c_6$$

$$G([i,j],[i+1,j]) = r_3(t) \cdot f_1(j, B_{50}), \quad G([i,j],[i,j+1]) = j \cdot c_5$$

where $r_3(t)$ is auto-inhibited by the total number of bulbous tips through the feedback function $f_1(j, B_{50}) = B_{50}/(j + B_{50})$. The resulting fit for the wild type is shown in Figure 1H (solid lines), showing that this model can capture the observed bulbous tip dynamics much better than model I. Essentially, model II results in few non-synaptogenic bulbous tips and guarantees that at least one stabilized (synaptogenic) bulbous tip is present at all times, as observed for wild type. The biological mechanism behind this feedback could be a general resource limitation for factors stabilizing bulbous tips in combination with an allocation of this stabilizing resource to particular bulbous tips, which, in turn, prevents further bulbous tips to be stabilized, as described in the Results section and the computational test below.

Computational test whether resource limitation and a competitive advantage can give rise to "winner-takes-all"-dynamics

We set up a simple mechanistic model of seeding factor uptake and stabilization of bulbous tips (Figure S3) that allows to test the effects of (i) "*resource*"/*seeding factor limitation* and (ii) *competitive advantage* (seeding factor dependent stabilization of bulbous tips). First, we tested under what conditions the resource accumulated in bulbous tips in the model as experimentally observed (Figure 2). Our simulation results (Figure S4, left panels) indicate that "*resource*"/*seeding factor limitation* is a pre-requisite for the accumulation of seeding factors in bulbous tips. We then tested for all parameter configurations that passed this first test, whether the number of bulbous tips present per time instance agrees with the experimental data (Figure S4, right panels). This second test revealed that only in the case of "*resource*"/*seeding factor limitation* plus *competitive advantage* the model predictions agree with the experimental data. In sum, these computational experiments show that *resource limitation* and *competitive advantage* are sufficient to explain competitive 'winner-takes-all' dynamics without an additional active filopodial communication mechanism.

Synapse generation, r_6

As mentioned earlier we assumed first-order kinetics and in line with the serial synapse formation model assumed that only one bulbous can generate a synapse at a time, deriving

$$r_6 = c_6 \cdot \min(synB, 1)$$

Parameter $c_6 = 1/120$ (min^{-1}) was then approximated from the maximum slope of synapse generation presented in Figure 3F.

Wild type model and parameters

The reactions rate/propensities of the stochastic model are given by

$$r_{1,sF}(t) = f_F(t) \cdot c_{1,sF}, \quad r_{2,sF}(sF) = sF \cdot c_{2,sF}$$

$$r_{1,\ell F}(t) = f_F(t) \cdot c_{1,\ell F}, \quad r_{2,\ell F}(sF) = \ell F \cdot c_{2,\ell F}$$

$$r_3(t, sF, \ell F, B) = c_3(sF + \ell F) \cdot f_1(B, B_{50}) \cdot f_{FB}\left(t, t_{\frac{1}{2}}\right), \quad r_4(sB) = c_4 \cdot sB$$

$$r_5(sB) = c_5 \cdot sB, \quad r_6(synB) = c_6 \cdot \min(1, synB)$$

Using the methods explained in the previous sections, we derived the parameters depicted in the table below for the wild type. We first estimated $c_{2,sF}$, $c_{2,\ell F}$ from the filopodial lifetime data (Figure S9G). Using the mean number of *sF*, *ℓF* at P40 (Figures 1F,

S6D, S6E, S6J, and S6K) and (Figures S7D, S7E, S7J, and S7K), we then estimated $c_{1,sF}$, $c_{1,\ell F}$. Using these parameters and the measured slow-scale dynamics (Figure 3B), we fit the fifth-order polynomial $f_F(t)$. From the lifetimes of bulbous tips we estimated c_4, which we used together with the number distribution of short-lived and synaptogenic bulbous tips to estimate B_{50}, c_5 and $r_3(t)$ in the auto-inhibition model (model II, Figure 1H). Using all parameter estimates derived so far and setting $t_{1/2}$ = 1000 (min) in function $f_{FB}(t,t_{1/2})$, we estimated parameter c_3. All model parameters below are in units $(\text{min})^{-1}$, except for $t_{1/2}$ (min) an B50 (unit less).

	$c_{1,sF}$	$c_{2,sF}$	$c_{1,\ell F}$	$c_{2,\ell F}$	c_3	c_4	c_5	c_6	B_{50}	$t_{1/2}$
wt	3.88	0.69	1.15	0.11	0.022	1/120	0.1133	1/120	0.0282	1000
dlar	2.63	0.69	1.49	0.11	0.0072	0.3	0.0228	1/120	10^{-4}	1000
Liprin-α	3.12	0.69	0.99	0.11	0.0152	0.111	0.0028	1/120	0.363	1000
syd-1 Trio	2.84	0.69	1.07	0.11	0.0321	0.169	0.0048	1/120	1.084	1000
	4.71	0.69	1.61	0.11	0.0139	0.1311	0.1865	1/120	0.0231	1000

The fifth-order polynome $f_F(t) = \max(0, \sum_{i=0}^{5} p_i \cdot t^i)$ has coefficients $p_5 = -2.97 \times 10^{-14}$, $p_4 = 3.31 \times 10^{-13}$, $p_3 = -1.29 \times 10^{-9}$, $p_2 = 2.06 \times 10^{-6}$, $p_1 = -1.45 \times 10^{-3}$ and $p_0 = 1$. Parameter c_6 could not be determined from data and was set to 1/120 min (almost all wild type bulbous tips eventually become synaptogenic). Note that the *trio* feedback mechanisms was modeled slightly different as outlined in the methods section.

Mutant models and parameters. The lifetimes of short and long-lived filopodia were not markedly different between the mutants as shown below,

	Short-Lived			Long-Lived		
Mutant	P40	P60	P40 and P60	P40	P60	P40 and P60
wt	2.4(1.7)	1.9(1.4)	2.2(1.6)	18(13)	23(18)	20(15)
dlar	2.7(1.7)	2.3(1.5)	2.5(1.6)	23(17)	19(15)	22(16)
Liprin-α	2.6(1.9)	2.3(1.6)	2.5(1.8)	18(13)	20(15)	19(14)
syd-1	2.3(1.6)	2.2(1.7)	2.3(1.7)	18(13)	23(16)	20(14)
Trio	2.3(1.7)	2.6(1.8)	2.5(1.8)	19(12)	20(15)	20(14)

Where we depict the average (standard deviation) lifetime of filopodia (min) that were classified as short-lived vs. long-lived based on the 8 min criterium. Hence, rates $c_{2,sF}$, $c_{2,\ell F}$ were set equal for all mutants and wild type. By contrast, the number of short- and long-lived filopodia were different between wild type and mutants as shown below.

	Short-Lived		Long-Lived	
Mutant	P40	P60	P40	P60
wt	5.6(3.9)	3.4(1.8)	10(3.5)	4.9(2)
dlar	3.8(2.3)	2.2(1.7)	13(2.3)	5.2(1.6)
Liprin-α	4.5(2.7)	2.6(1.5)	8.6(2.1)	6.5(1.9)
syd-1	4.1(2)	1.6(1.3)	9.3(3.3)	3.8(1.7)
Trio	6.8(2.8)	4.5(2.2)	14(3.7)	10(2.7)

Average (standard deviation) numbers of short-lived and long-lived filopodia per time instance.

We modeled these differences by estimating mutant-specific rates $c_{1,sF}$, $c_{1,\ell F}$. We observed distinct populations of transient and stable bulbous tips in all mutants (Figures S9A–S9E). Consequently, parameters c_4 were set to the inverse of the mutant-specific bulbous tip life times (average (standard deviation) life time of transient bulbous tips sB in min; *dlar*: 3.3 (3), *lirin-α*: 9 (9.6), *syd-1*: 5.9 (6.4), *trio*: 7.6 (6.6) and *wt*: set to 120 min as it could not be determined from the data). *Trio*, unlike the other mutants, exhibited at least one stabilized (synaptogenic) bulbous tip at all time points. The data measured suggest that *trio* may be a negative regulator of bulb initiation, such that bulbous initiation is more frequent in the *trio* mutant, while stabilization is essentially unaffected by *trio*. This observation prompted us to assume a strong auto-inhibitory feedback mechanisms of synaptogenic bulbous tips on their own production. The generator for this model is as follows:

$$G([i,j],[i-1,j]) = i \cdot c_4, \quad G([i,j],[i,j-1]) = j \cdot c_6$$

$$G([i,j],[i+1,j]) = r_3(t), \quad G([i,j],[i,j+1]) = j \cdot c_5 \cdot f_1(j, B_{50})$$

with parameters stated in the table in the section **Wild type model and parameters** above.

Simulation of growth cone retraction. Figure 6 shows the simulated probability of growth cone retractions up to time T, $P_{retract}(T)$ based on the idea that both filopodia and synapses contribute to axon terminal stabilization. The probability of growth cone retraction was computed as

$$P_{\text{retract}}(T) = 1 - \prod_{i=0} P_{\text{no-retract}}(i)$$

Where $P_{no-retract}(i)$ denotes the probability not to retract in the ith time interval which is computed by $P_{\text{no-retract}}(i) = e^{-\Delta t \cdot r_o \cdot f_{retract}(F(i),B(i),S(i),w,n_{stab})}$, where r_0 is the basal rate of retraction, Δt is the duration of the ith time interval and F(i), B(i), S(i) are the simulated number of filopodia, bulbous tips and synapses during that time interval. n_{stab} is the 'minimal stabilization number' and w are the user-defined weights such that

$$f_{\text{retract}}(F(i), B(i), S(i), w, n_{stab}) = 0.5\left(1 + \tanh\left[\frac{3}{n_{stab}}(n(i) - n_{stab})\right]\right)$$

with $n(i) = w_f(sF + \ell F) + w_B(sB + synB) + w_s \cdot S$ being the weighted sum of filopodia, bulbous tips and synapses affecting (preventing) retraction.

DATA AND CODE AVAILABILITY

Raw (.lif format) and processed (.ims and .am format) imaging datasets are available on request.

The filopodia tracking software is an extension of the commercial software Amira, which is available from Thermo Fisher Scientific. The filopodia tracking software is available from the corresponding author upon request in source code and binary form. Executing the binary requires a commercial license for Amira.

MATLAB codes for model parameter inference and for model simulation are available through https://github.com/vkleist/Filo along with tracked filopodia data used for parameter inference.

Developmental Cell, Volume *50*

Supplemental Information

Serial Synapse Formation through Filopodial Competition for Synaptic Seeding Factors

M. Neset Özel, Abhishek Kulkarni, Amr Hasan, Josephine Brummer, Marian Moldenhauer, Ilsa-Maria Daumann, Heike Wolfenberg, Vincent J. Dercksen, F. Ridvan Kiral, Martin Weiser, Steffen Prohaska, Max von Kleist, and P. Robin Hiesinger

Supplementary Figures and Table

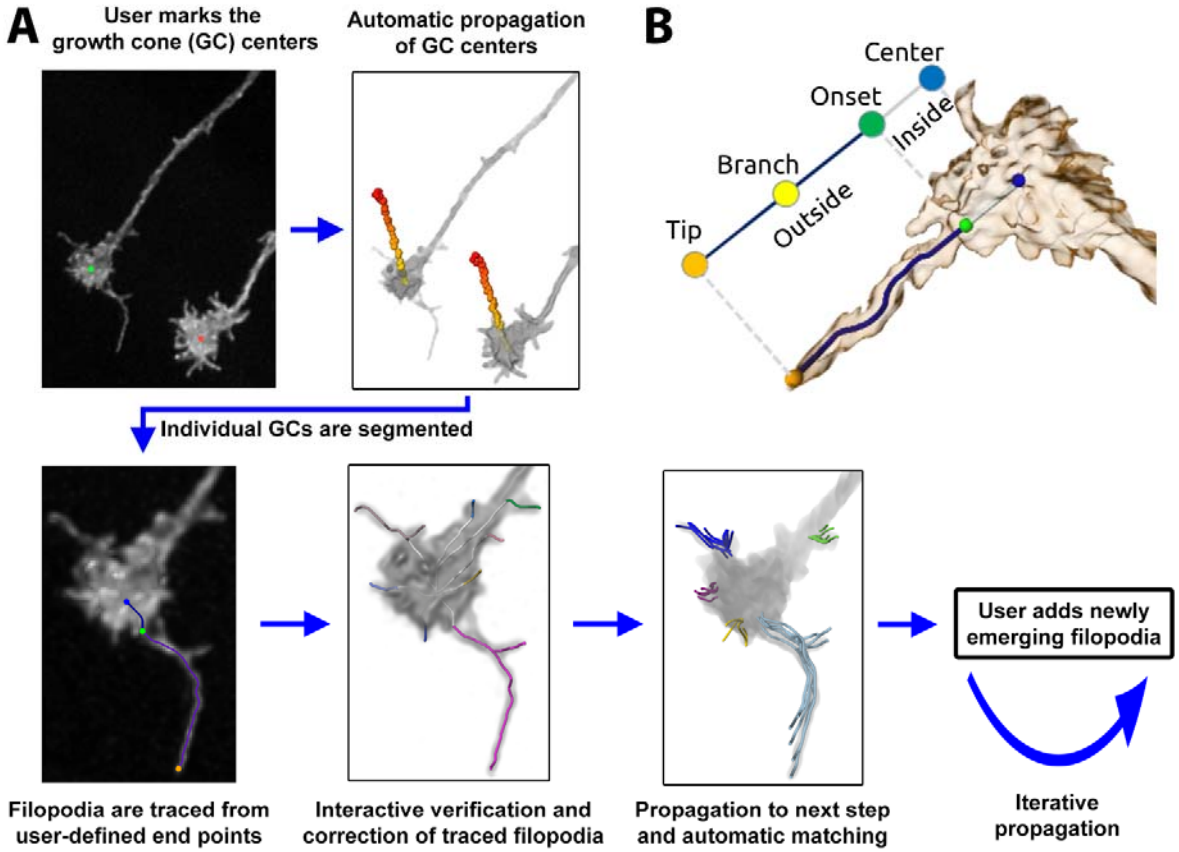

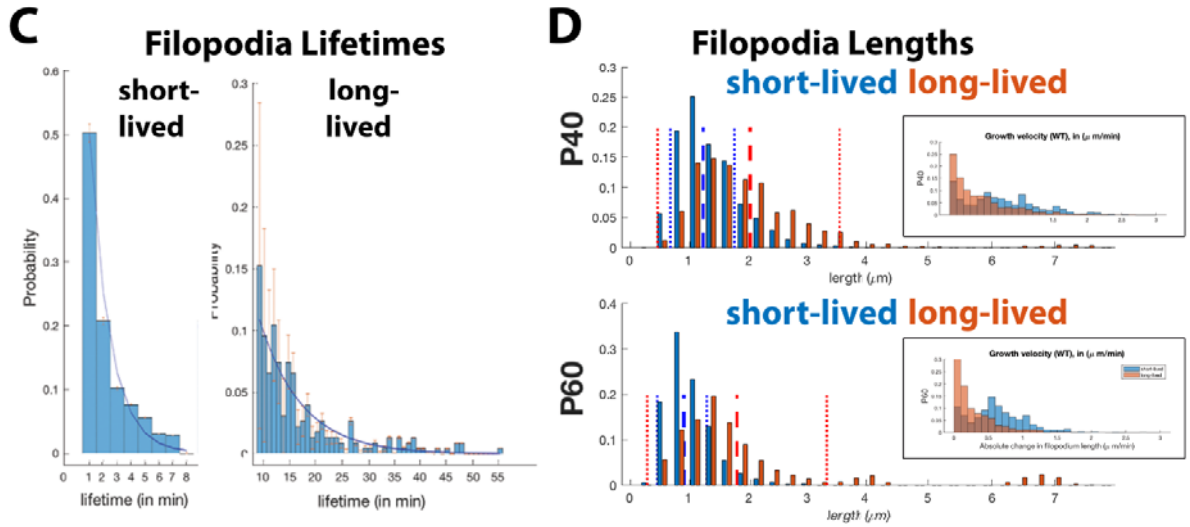

Figure S1: Filopodia quantification. Related to Figure 1. (A) The user selects the growth cone (GC) for further processing by marking the centers (color-coded) in the first timestep. Their successors are automatically detected in the following time steps. To process the GCs one at a time, the user adds a new filopodium by interactively specifying the tip (orange). The path to the GC center (blue) is then automatically traced. The filopodia onset (green) is set to the location on the path where the intensity profile in a plane orthogonal to the path changes from Gaussian to non-Gaussian. The onset point divides the path into an inside (blue) and an outside (purple) part, the latter being the actual filopodium. A different track ID (color-coded) is assigned to each filopodium. **(B)** A neuronal growth cone is represented as a skeleton graph (tree). One branch of the tree extended from the GC center (blue) to the filopodia tip (orange), passing through the onset location (green) and potentially branching nodes (yellow). The part of the path between tip and onset ("Outside") is the actual filopodium. **(C)** All filopodial lifetimes can be described with two exponential distributions, one for short-lived and one for long-lived filopodia. **(D)** Filopodial length distributions can be described with separate distributions for short-lived and long-lived filopodia, both for P40 and P60.

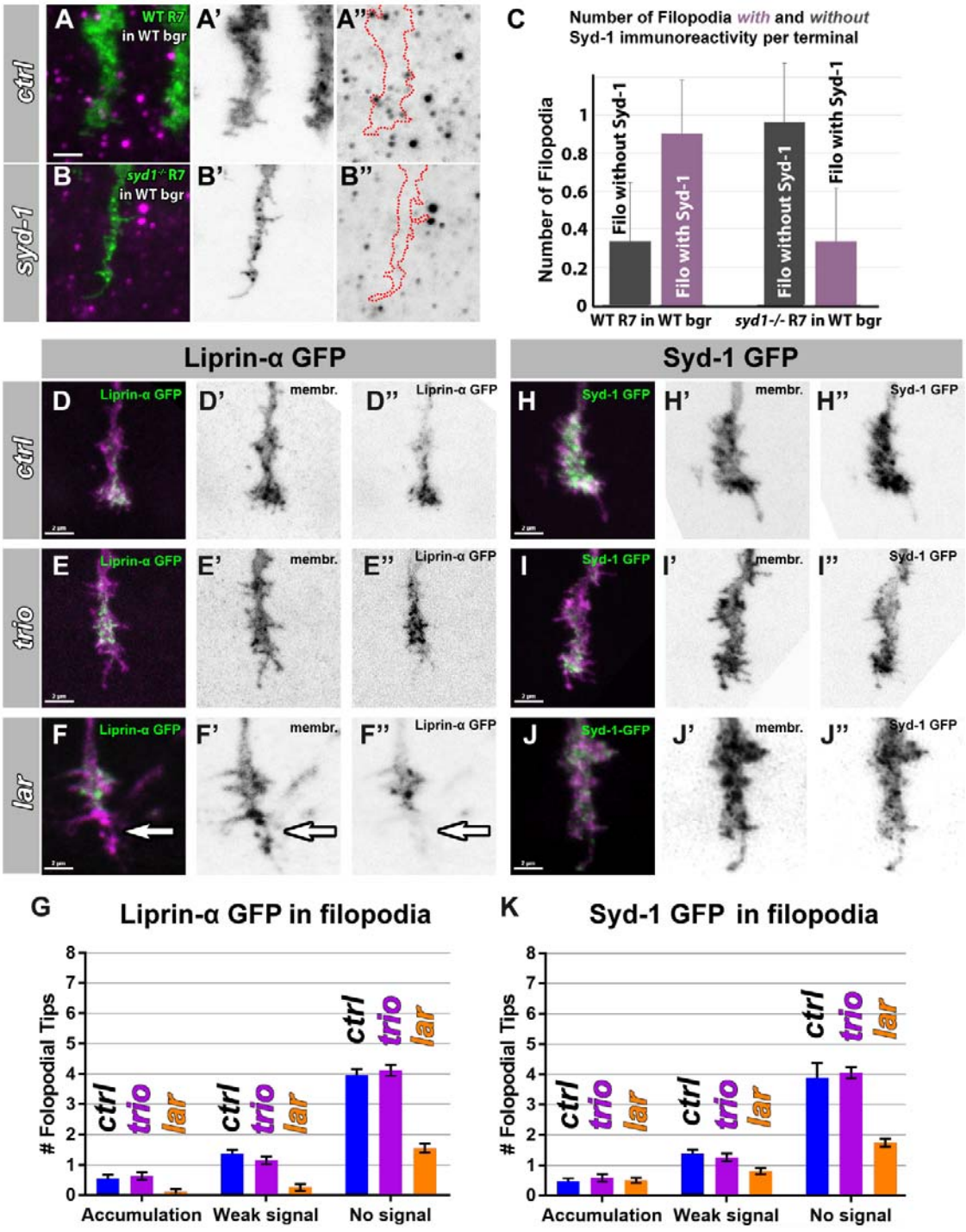

Figure S2: Endogenous Syd-1 in axon terminals and Liprin-α-GFP and GFP-Syd-1 in *lar* and *trio* mutant R7 axon terminals. Related to Figure 2. (A) Syd-1 (magenta) in a wild type brain with a wild type single GFP-marked R7 axon terminal. **(B)** Syd-1 labeling in a wild type brain with a single *syd-1* mutant, GFP-labeled R7 axon terminal.

Note that each region contains many other Syd-1-expressing neurons that are partially overlapping with the positively labelled R7 axon terminals. **(C)** Quantification of the presence of Syd-1 immunoreactivity in filopodia reveals a selective loss of signal in filopodia of syd-1 mutant R7 axon terminals. Scale bar in (A) for (A-B): 2um. Error bars: standard deviation. **(D-K)** Analyses of Liprin-α-GFP and GFP-Syd-1 in *lar* and *trio* mutant R7 axon terminals**. (D-F)** Liprin-alpha-GFP localization in wild type, trio and lar mutant terminals. **(H-J)** GFP-Syd-1 localization in wild type, trio and lar mutant R7 terminals. Quantification of Liprin-α-GFP **(G)** and Syd-1-GFP **(K)** detection in filopodia. Arrow in (C) marks filopodial region without Liprin-α in *lar* mutant terminal.

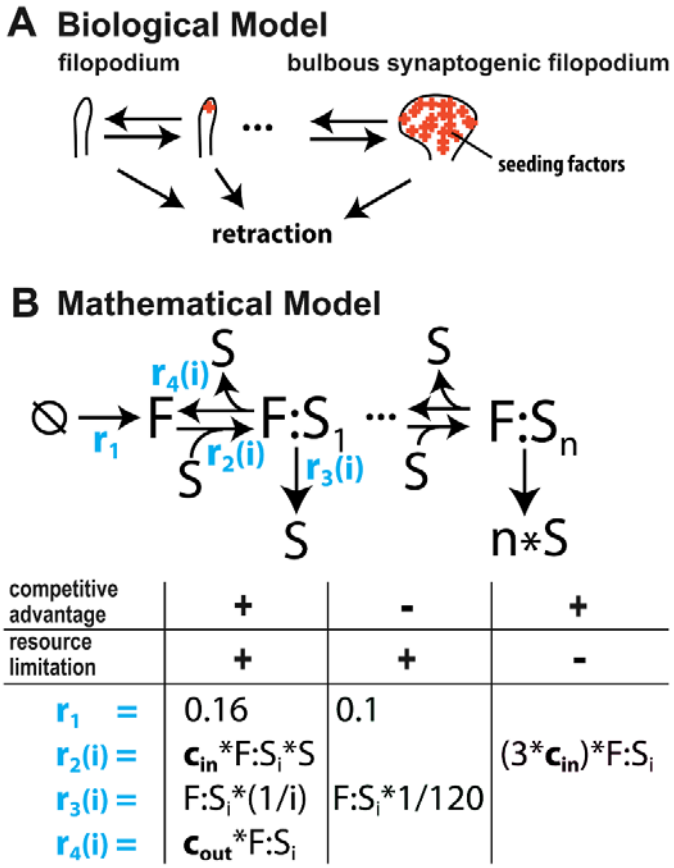

competitive advantage	+	-	+
resource limitation	+	+	-
r_1 =	0.16	0.1	
$r_2(i)$ =	c_{in}*F:S_i*S		(3*c_{in})*F:S_i
$r_3(i)$ =	F:S_i*(1/i)	F:S_i*1/120	
$r_4(i)$ =	c_{out}*F:S_i		

Figure S3: Biological first principles that explain 'winner-takes-all' dynamics. Related to STAR Methods. A: We assume a simple biological model in which seeding factors and other proteins (the resource; red crosses) accumulate in filopodial tips, whereby filopodial tips become more bulbous-like, the more resources (seeding factors and other proteins) accumulate (up to some maximum number *n*). **B**. Corresponding mathematical model to test the predictions of 'resource limitation' (restriction of how many resource proteins are available) and a 'competitive advantage' of those tips that accumulate the resource. Specifically, we tested whether 'winner-takes-all' dynamics require a competitive advantage. In the model new filopodia emerge (reaction r_1), accumulate resources (reaction r_2), retract (reaction r_3) or release resources (reaction r_4). The model has two free parameters (c_{in} and c_{out}) that describe the rate at which resources are accumulated vs. released from filopodia. We will test the two parameter settings: $c_{in} \leq c_{out}$ (parameter set I) and $c_{in} > c_{out}$ (parameter set II).

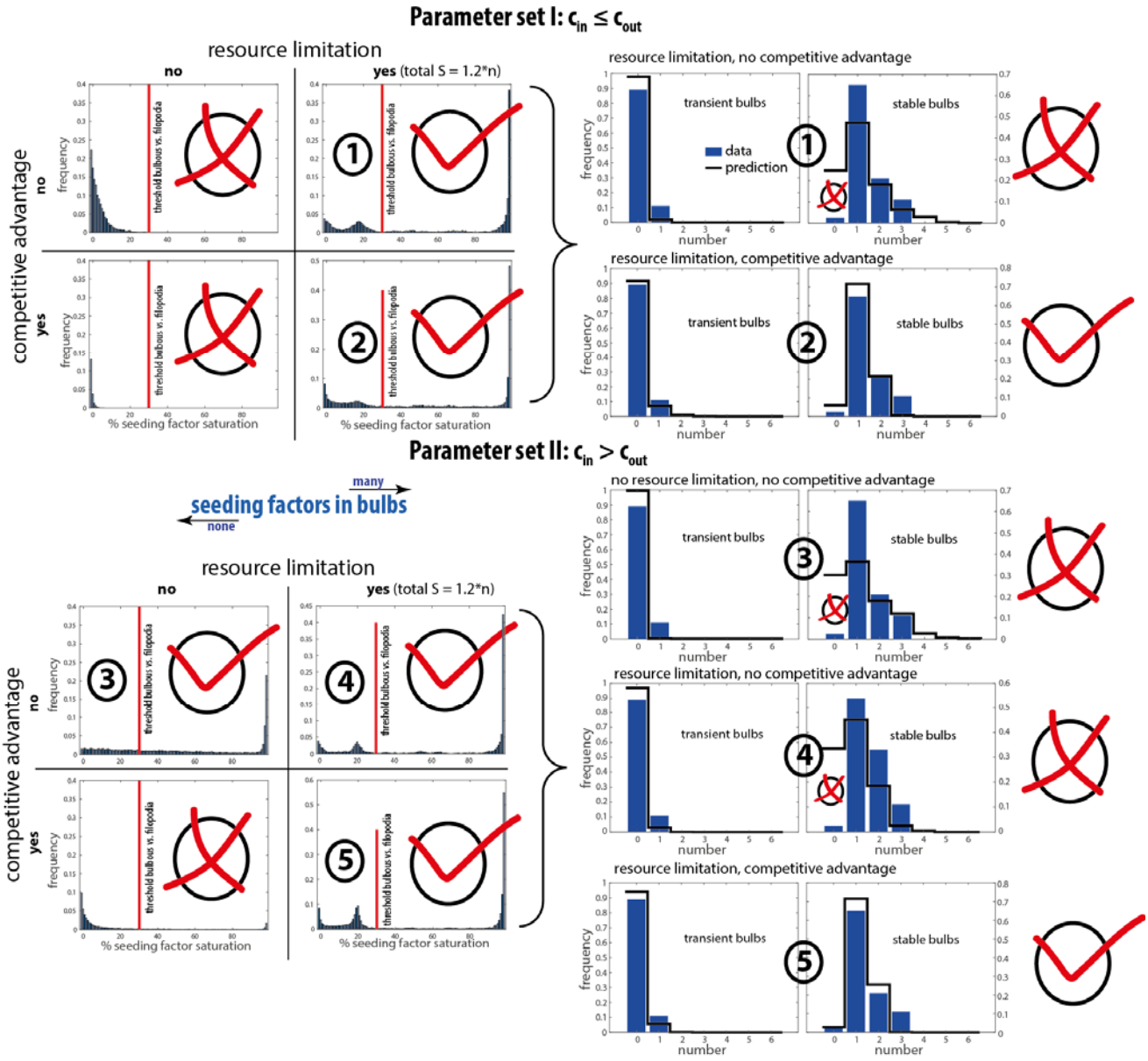

Figure S4: Computational test whether 'resource limitation' and 'competitive advantage' explains seeding factor accumulation and bulbous tip distribution. Related to STAR Methods. For the two parameter settings (parameter set I: $c_{in} \leq c_{out}$, parameter set II: $c_{in} > c_{out}$) we stochastically simulated the model depicted in Fig. S3B using different assumptions (resource limitation, competitive advantage). **Left panels**: We tested whether seeding factors accumulate in only a few bulbous filopodia (compare Fig. 2, main manuscript). The bars indicate the computed frequency of bulbous tips that have accumulated either very few seeding factors (left bars) vs. very many (close to their

maximum capacity, right bars) at steady state. Only in the models marked with symbols ①-⑤ we observe that seeding factors correctly accumulate in particular bulbous tips.

Right panels: We then tested whether models ①-⑤ also explain the bulbous tip distribution, where the solid black lines indicate the simulated bulbous tip distribution and the blue bars are the experimentally observed distribution in the wildtype (compare Fig. 1H). As can be seen, only the scenario where we have both ‘resource limitation’ and a ‘competitive advantage’ yields a bulbous tip distribution that is in line with the experimentally observed distribution in the wildtype, irrespectively of the parameter setting.

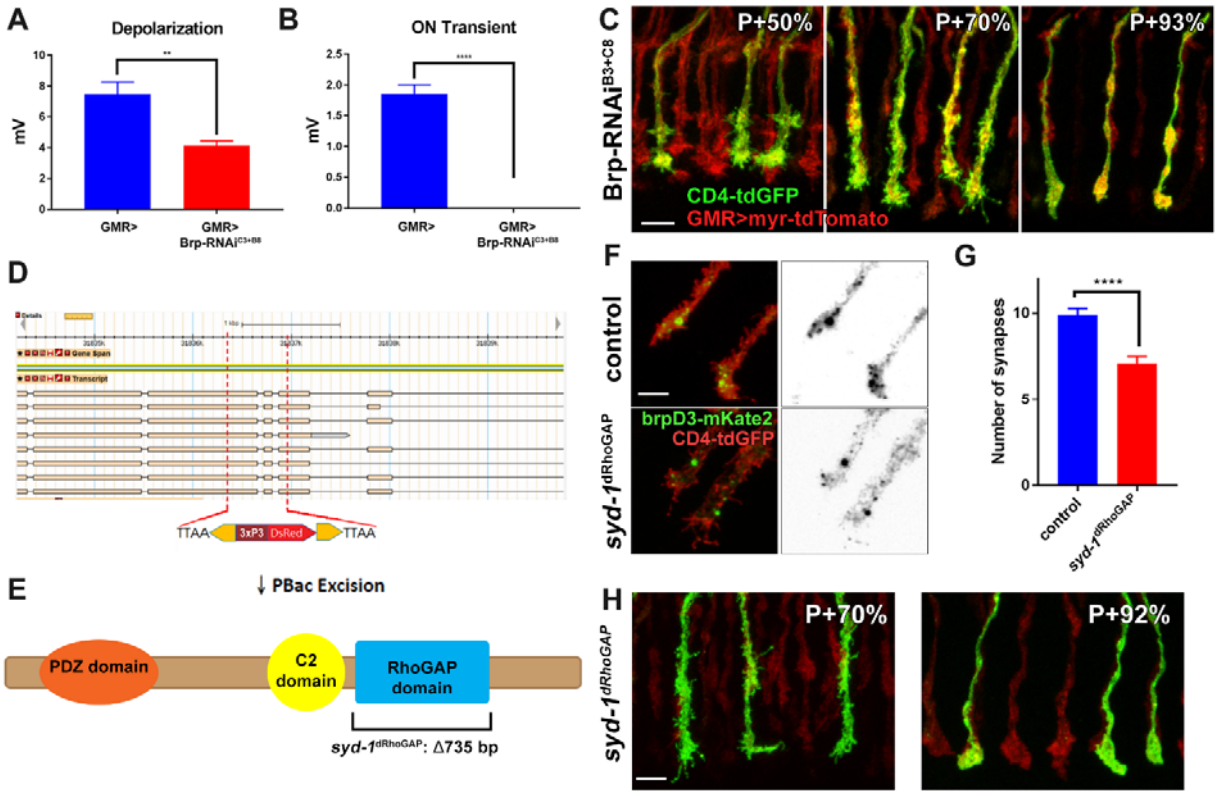

Figure S5: Mutant analyses: Bruchpilot and the RhoGAP domain of Syd-1 are not required for normal development of R7 axons. Related to Figure 4. (A-C) Brp mutant analyses. ERG recordings showing the level of **(A)** depolarization (p = 0.0014) and **(B)** ON Transient (p<0.0001) from eyes that express only GMR-Gal4 and those that co-express two RNAi constructs against the *brp* gene, Brp-RNAiB3 and Brp-RNAiC8. Error bars denote SEM. **(C)** Sparsely generated R7 clones during pupal development are labeled with CD4-tdGFP and co-express the two RNAi constructs. All photoreceptors are marked with myr-tdTomato. **(D)** CRISPR-mediated, scarless knock-in of the construct into the *syd-1* locus. Upon PBac excision of the DsRed casette **(E)** RhoGAP domain of Syd-1 is deleted completely and specifically, leaving the rest of the protein intact. **(F)** Presynaptic punctae at P+70% in sparsely generated *syd-1dRhoGAP* R7 terminals and FRT82B controls. **(G)** Quantification of b (n= 45 and 32, p<0.0001) **(H)** Sparsely generated *syd-1dRhoGAP* clones marked with CD4-tdGFP and all photoreceptors marked with myr-tdTomato. Mutant axons appear normal at P+70% and 92%. Scale bars: 5 µm.

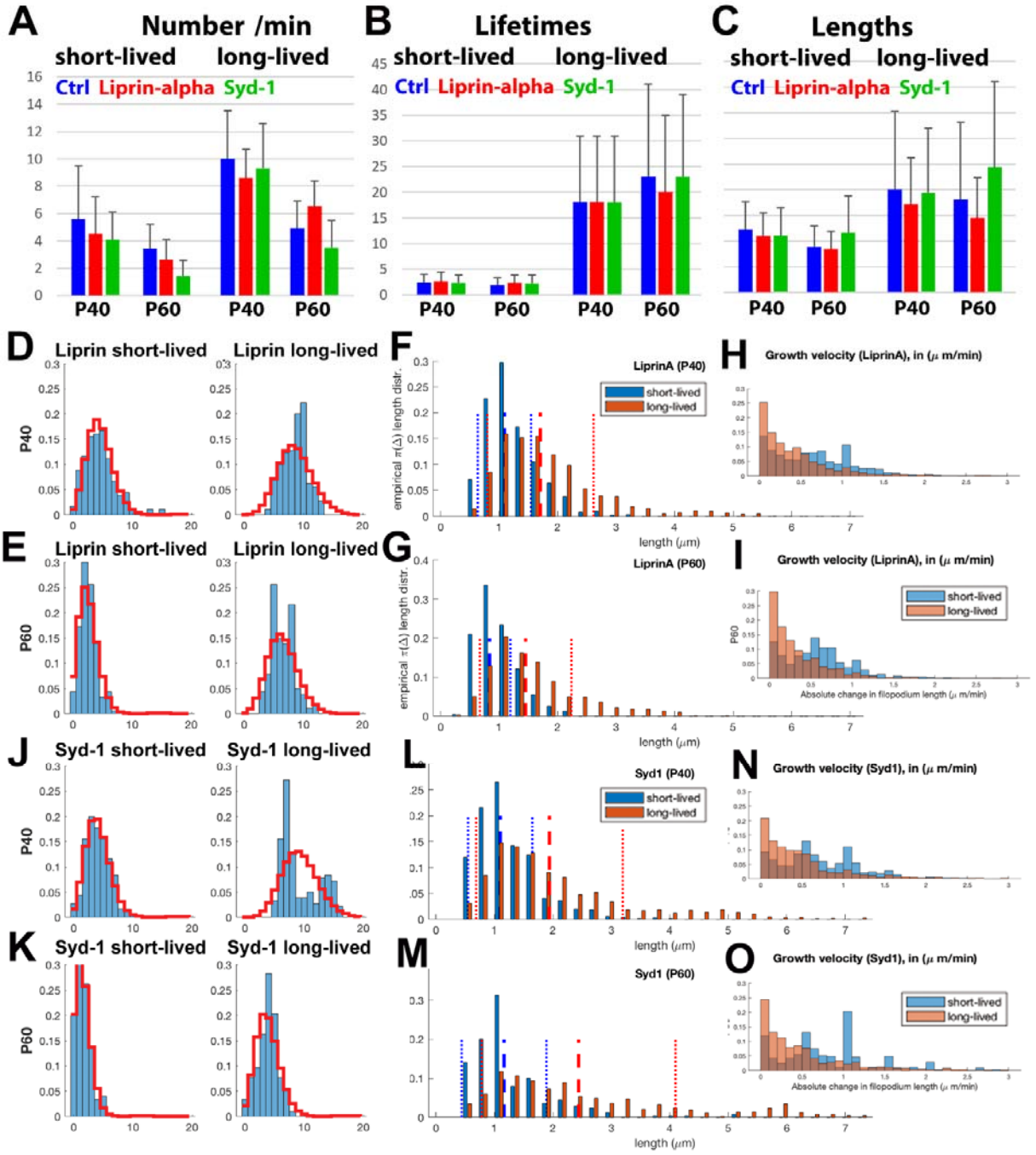

Figure S6: Number, lifetime, length and velocity statistics for filopodia in liprin-α and syd-1 mutants. Related to Figure 4. (A-C) Numbers, lifetimes (min) and lengths of short-lived and long-lived filopodia at both P40 and P60 are not statistically different in ctrl, *liprin-α* and *syd-1*. **(D-E)** Numbers of short-lived (left) and long-lived (right) filopodia in the *liprin-α* mutant resemble Poisson distributions. **(F-I)** Lengths and velocity

distributions of short-lived and long-lived filopodia in the *liprin-α* mutant resemble Poisson distributions. **(J-K)** Numbers of short-lived (left) and long-lived (right) filopodia in the *syd-1* mutant resemble Poisson distributions, except for some long-lived filopodia at P40. **(L-O)** Lengths and velocity distributions of short-lived and long-lived filopodia in the *syd-1* mutant resemble Poisson distributions except for a few particularly long, long-lived filopodia.

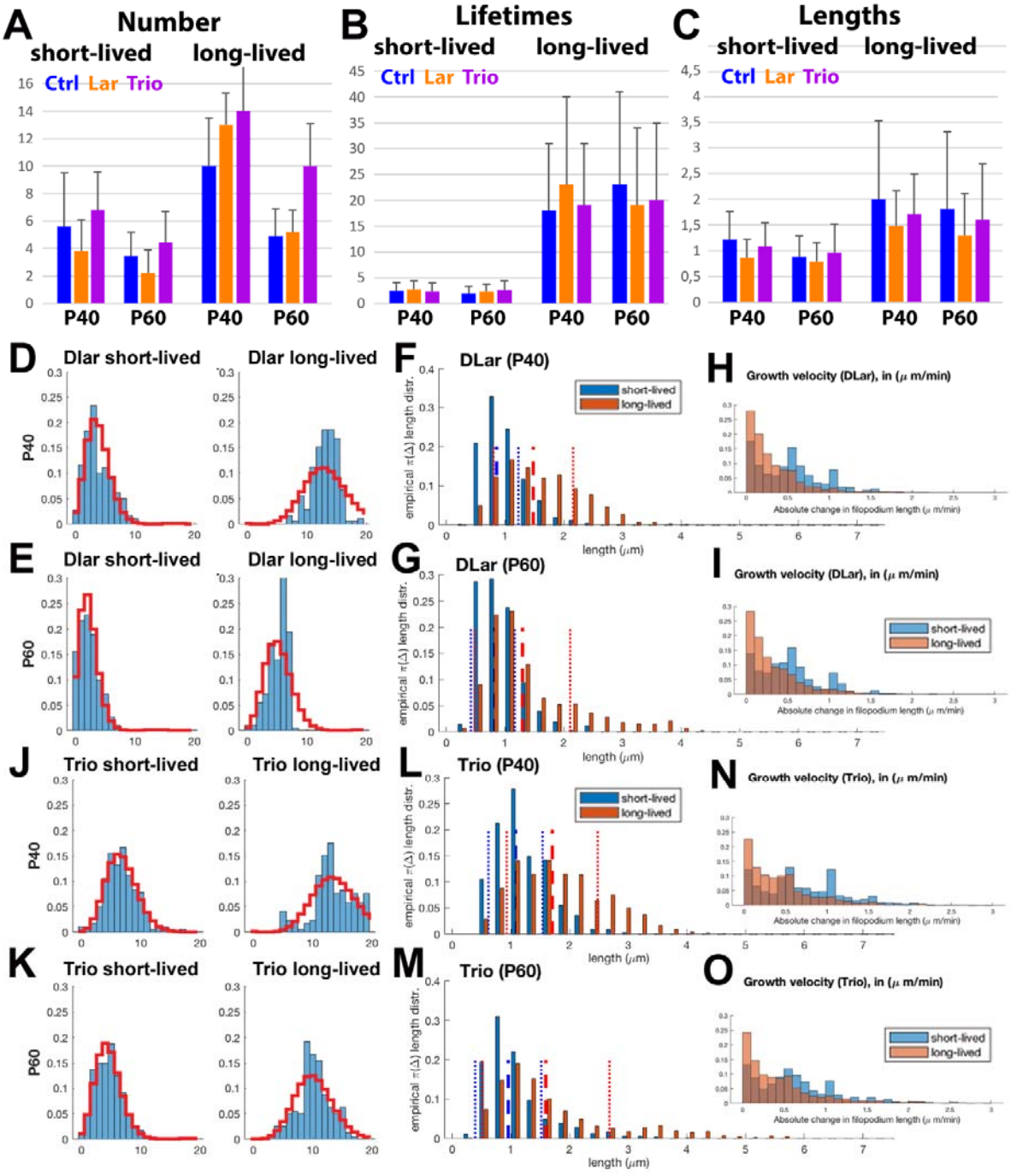

Figure S7: Number, lifetime, length and velocity statistics for filopodia in lar and trio mutants. Related to Figure 5. (A-C) Numbers, lifetimes and lengths of short-lived and long-lived filopodia at both P40 and P60 are not statistically different in ctrl, *lar* and *trio*, except for mild increases of filopodia numbers in trio at P60. **(D-E)** Numbers of short-

lived (left) and long-lived (right) filopodia in the *lar* mutant resemble Poisson distributions. **(F-I)** Lengths and velocity distributions of short-lived and long-lived filopodia in the *lar* mutant resemble separate Poisson distributions. **(J-K)** Numbers of short-lived (left) and long-lived (right) filopodia in the *trio* mutant resemble Poisson distributions. **(L-O)** Lengths and velocity distributions of short-lived and long-lived filopodia in the *trio* mutant resemble separate Poisson distributions.

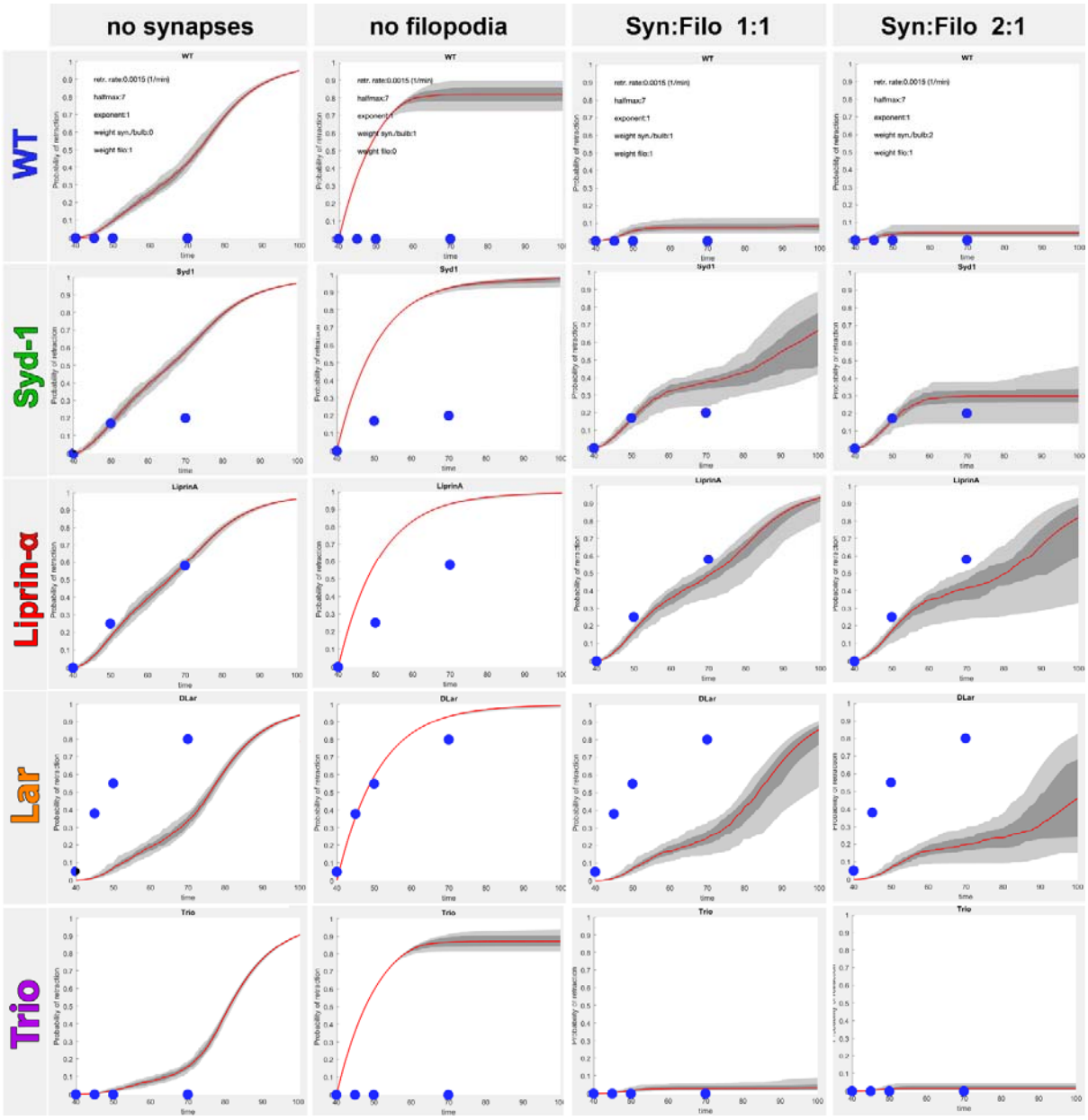

Figure S8: Modeling of retraction probabilities as a function of stabilization through filopodia and synapses. Related to Figure 6.

First column (left): Simulation of retractions if synapses do not contribute to axon terminal stabilization (but only filopodia stabilize terminals). All mutants would exhibit retractions after P50 if synapses do not contribute to stabilization.

Second column: Simulation of retractions if filopodia do not contribute to axon terminal stabilization (but only synapses stabilize terminals). Retractions would be similar in all mutants due to absence of synapses before P50.

Third column: Simulation of equally weighted filopodia and synapses contributing to axon terminal stabilization. Wild type and *trio* exhibit no retractions, as declining filopodia numbers are compensated for by increasing synapse numbers. lar, *liprin-α* and *syd-1* exhibit retractions with different kinetics based on defects in synapse formation.
Fourth column (right): Simulation of stabilization weighted 2:1 to synapses over filopodia only mildly changes retraction dynamics and matches closely the observed retraction kinetics in all mutants except *lar*. *lar* is best matched if filopodia do not contribute to stabilization (second column), suggesting a loss of filopodial adhesion as well.
Blue discs: measured retraction values.

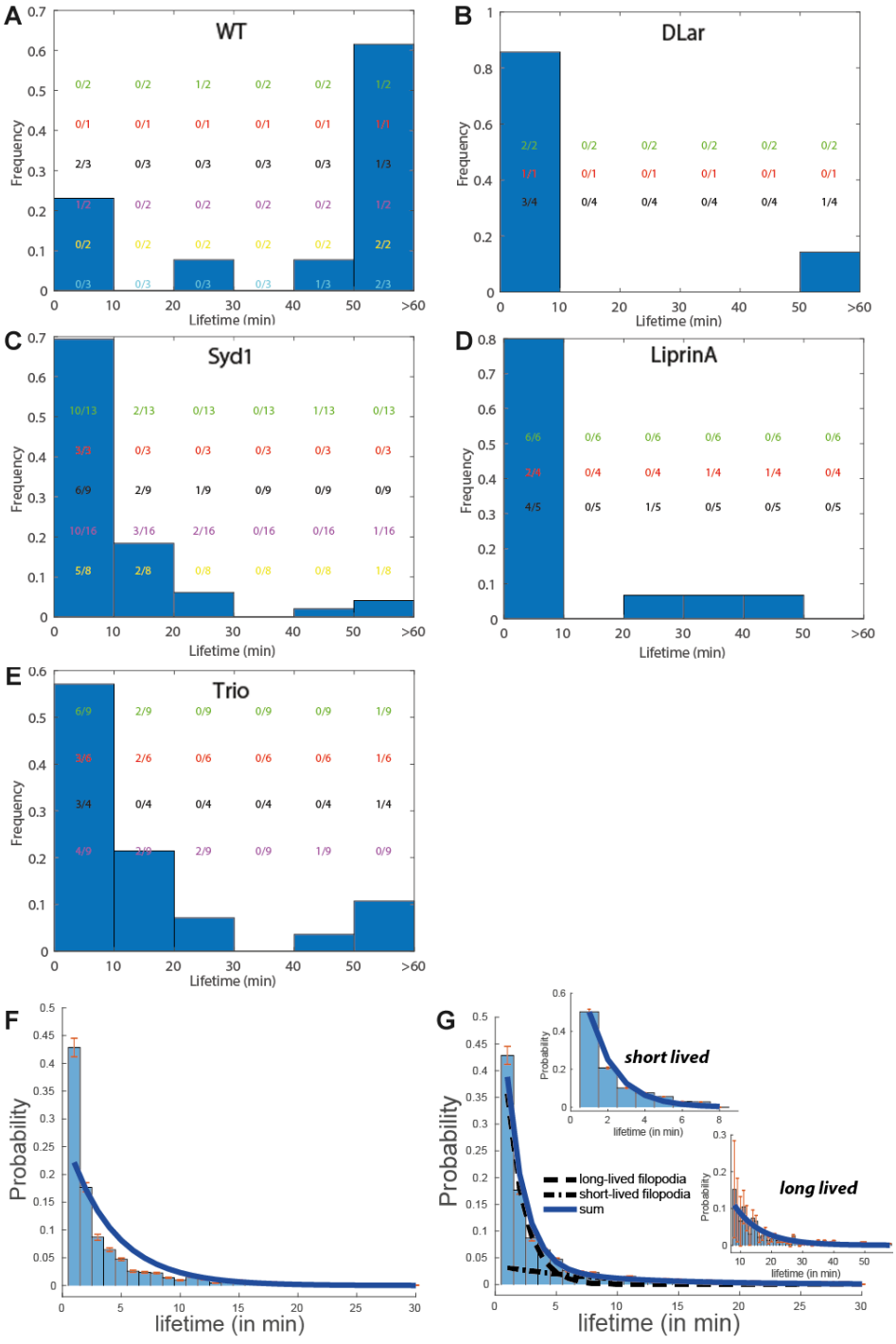

Figure S9: Bulbous tip life time distribution and identification of two filopodia subpopulations. Related to STAR Methods. A Wild type exhibits 2-3-times less short-lived bulbous tips than long-lived bulbous tips. By contrast, all mutants **(B-E)** exhibit a several-fold increased population of short-lived bulbous tips (left bars) and

similarly reduced populations of long-lived bulbous tips. Numbers show the counts in each life time category for different growth cones.

(F-G) Blue bars indicate the measured filopodia lifetime distribution from individual filopodia recordings at P40 and P60 respectively. **F**. The thick blue line indicates the best fit based on a single filopodium population with an exponential lifetime. Neither the large number of very short-lived filopodia nor the few very long-lived filopodia are well represented. **G.** The thick blue lines indicate the best fits for two filopodia subpopulations with distinct exponential lifetimes. The short-lived filopodia (sF) retract with rate constant 0.69 (min^{-1}), whereas the fast filopodia retract with rate 0.12 (min^{-1}).

Table S1. Rates of bulbous filopodia dynamics at P60. Related to Figure 3.

	r3	r2B	E[f1]	r4	r5	Avg. bulbs
WT	0.0222 (0.0172)	0.1636	0.0768	0.0083	0.0117	1.5300
Liprin	0.0833 (0.0167)	0.0949	0.8347	0.0778 (0.0255)	0.0019	0.9526
Syd1	0.16 (0.0847)	0.2049	0.7737	0.1533 (0.0767)	0.0044	1.4296
Lar	0.0333(0.0167)	0.0576	0.6736	0.0333 (0.0167)	0.0027	0.4477
Trio	0.1125 (0.0438)	0.1381	1.0000	0.1 (0.0408)	0.0141	1.6331

r3: measured rate of bulb formation, contains r2B * f1, unit: 1/min
r2B: propensity to form bulbs, cannot be measured, because feedback f1 reduces r2B, shown is the only possible fit of r2B, unit: 1/min
f1: negative feedback on bulb formation, cannot be measure, see r5, shown is the only possible fit of the data (r2B; smaller f1 indicates stronger feedback; f1=1 indicates no feedback
r4: measured rate of bulbs disappearance, unit: 1/min
r5: measured rate of bulb stabilization, unit: 1/min
Avg. bulbs: average number of bulbs per time instance (min) over an hour (P60)
In blue: direct measurements; in brackets: Standard Deviation